Eur. Phys. J. C manuscript No.
(will be inserted by the editor)

Radial pulsations of gravitationally decoupled anisotropic self-bound stars with a generalized linear equation of state

D. Santana [a,1], **C. Usca**[b,1], **J. Andrade**[c,1], **J. O. Cedeño**[d,1,2]

[1]Escuela Superior Politécnica de Chimborazo, (ESPOCH), Riobamba 060155, Ecuador
[2]Centro de Investigación y Desarrollo Científico Zétesis, Ecuador

arXiv:2610.39346v1 [gr-qc] 29 Oct 2026

Received: date / Accepted: date

Abstract We construct anisotropic self-bound stellar configurations through gravitational decoupling in the minimal geometric deformation framework and investigate their stability against linear radial perturbations. Retaining the Tolman IV temporal potential, we impose the generalized linear equation of state $P_r = \eta(\rho - \rho_s)$ on the complete matter distribution. Central regularity and Schwarzschild matching determine the radial geometry and relate the surface density to the compactness and stellar radius. Closed-form solutions are obtained for $\eta = 1, 1/2, 1/3, 1/4$, including the MIT bag radial relation when $\eta = 1/3$ and $\rho_s = 4B$. Since the equilibrium anisotropy does not determine its dynamical response, we introduce two material prescriptions that preserve either the anisotropy of each fluid layer or its ratio to $\rho + P_r$. Including metric perturbations, we compute the fundamental mode and three overtones for twelve equilibrium configurations under both prescriptions. All 24 background response combinations have positive fundamental squared frequencies, establishing linear radial stability within the adopted closures. The fundamental eigenvalue decreases with compactness within each sampled family, while changing the anisotropic response produces shifts whose direction depends on the background. Tangential tensions in several configurations and the failed tangential profile diagnostic of the maximally stiff family limit their physical interpretation. These results provide analytically tractable self-bound backgrounds and demonstrate that identical equilibrium configurations can support distinct radial spectra depending on their anisotropic material response.

[a]e-mail: diego.santana@espoch.edu.ec
[b]e-mail: icrisus25@gmail.com
[c]e-mail: julio.andrade@espoch.edu.ec
[d]e-mail: jorge.cedeno@czetesis.com

Keywords: Self-bound stars; Pressure anisotropy; Gravitational decoupling; Minimal geometric deformation; Linear equation of state.

1 Introduction

Compact stars constitute unique astrophysical laboratories for investigating the behaviour of matter and gravity under conditions that cannot be reproduced in terrestrial experiments [1]. Their interiors may reach densities several times higher than the nuclear saturation density ($\sim 2.7 \times 10^{17}\,\mathrm{kg\,m^{-3}}$ in mass-density units [2]), where the microscopic composition of matter remains uncertain and a wide variety of phases may arise, including hyperonic matter, meson condensates, deconfined quarks, color-superconducting phases, and other strongly interacting states [3–7]. The macroscopic properties of these objects, such as their masses, radii, compactness, tidal response, and oscillation spectra, depend strongly on the equation of state (EoS) governing the stellar interior. Consequently, constructing relativistic stellar models that connect the microscopic properties of dense matter with potentially observable quantities remains one of the central problems of modern gravitational physics and high-energy astrophysics.

For a fixed EoS, the central density typically increases with gravitational mass along a connected stable branch of nonrotating stellar configurations, making massive pulsars particularly valuable for probing matter under extreme conditions. Among the landmark measurements is that of PSR J1614−2230, whose mass was initially determined to be $1.97 \pm 0.04\,M_\odot$ using Shapiro delay [8] and subsequently refined to $1.928 \pm 0.017\,M_\odot$ in the NANOGrav nine-year analysis [9]. Another important measurement is that of PSR

J0348+0432, with $2.01 \pm 0.04\,M_\odot$ [10]. The existence of compact stars with masses close to or above two solar masses places strong constraints on the EoS, which must provide sufficient pressure at supranuclear densities to prevent gravitational collapse [11].

While the maximum mass of a compact star is mainly determined by the behaviour of matter in its high-density core, the radii of predominantly nucleonic neutron stars with canonical masses of approximately 1.3–1.5 $M_\odot$ are particularly sensitive to the pressure around and above nuclear saturation density, and hence to the density dependence of the nuclear symmetry energy [6]. Precise radius measurements are therefore essential for constraining dense matter, although their interpretation depends on the observational method and on assumptions concerning thermal emission, stellar atmospheres, source distance, geometry, and X-ray pulse profiles. The NICER mission [12] has provided mass–radius constraints through pulse-profile modelling, including analyses of PSR J0740+6620 [13,14]. The scientific cases for X-ray mission concepts such as Athena+ and LOFT have also emphasized the potential of high-throughput spectroscopy and timing for studying compact objects [15, 16]. Complementary information has been obtained from the multimessenger observation of GW170817 and its associated kilonova [17], while analysis of the gravitational-wave signal has constrained tidal deformabilities and the dense-matter EoS [18]. Nevertheless, such macroscopic constraints do not by themselves provide a unique identification of the stellar composition: hybrid stars can have mass–radius relations resembling those of hadronic stars [19], and self-bound quark-star models have also been constructed that satisfy mass, radius, and tidal constraints [20]. This motivates the investigation of complementary diagnostics, including oscillation spectra and dynamical stability [21–23].

Strange quark stars constitute a theoretically motivated, although still hypothetical, class of compact objects [7, 24, 25]. Their possible existence is based on the Bodmer–Witten hypothesis, according to which bulk matter composed of up, down, and strange quarks may be absolutely stable and represent the true ground state of strongly interacting matter [26–28]. Unlike ordinary neutron stars, which are bound primarily by gravity, strange quark stars would be self-bound by strong interactions and could retain a finite density at zero pressure, leading to distinctive internal structures and mass–radius relations [3, 7, 24, 25]. Historically, radius estimates for sources such as SAX J1808.4−3658 and RX J1856.5−3754 motivated interpretations in terms of strange or quark stars [29, 30]; these proposals should not be regarded as conclusive identifications. Deconfined quark matter may instead be confined to the cores of hybrid stars [31], whose equilibrium mass–radius relations can closely resemble those of purely hadronic stars [19]. Conversion to quark matter has also been proposed as an energy source in models of superluminous supernovae [32] and gamma-ray bursts [33]. Other proposed signatures concern gravitational waves from compact-star mergers [34], thermal evolution [35], and stellar oscillations [21–23].

The macroscopic description of self-bound quark matter commonly employs the MIT bag model or generalized linear and constant-speed-of-sound equations of state [28, 31, 36–38]. Although phenomenological, these models capture essential features of dense quark matter, including its stiffness and finite surface density, while allowing different physical regimes to be explored within a unified framework. A generalized linear EoS is particularly useful because it can reproduce the simplest MIT bag relation, approach the causal stiffness limit, or interpolate between softer and stiffer self-bound phases. It therefore provides a flexible basis for studying how the properties of dense matter influence the mass, radius, compactness, oscillation spectrum, and stability of strange quark stars without restricting the analysis to a single microscopic model.

Most relativistic stellar models treat matter as a perfect fluid, with the same pressure in every direction. This is a useful starting point, but it may leave out stresses associated with the internal structure of strange quark stars. Strong magnetic fields and crystalline phases, for example, can introduce preferred directions and allow the radial and tangential pressures to differ. Phase boundaries, density gradients, and the coexistence of different forms of matter may also contribute, depending on their microscopic properties. Pressure anisotropy thus has physical motivations, although its presence and magnitude must be assessed for the particular model rather than inferred from high density alone [39–45]. A related issue arises during gravitational collapse: studies of spherically symmetric dissipative fluids show that dissipative fluxes, density inhomogeneities, and shear can disturb an initially isotropic pressure distribution [46]. These results provide a further reason to examine anisotropic models, but they do not establish a universal anisotropic end state for compact stars..

When radial and tangential pressures differ, their difference contributes to the force balance inside the star. A tangential pressure greater than the radial pressure provides an outward contribution, whereas the reverse produces an inward one. This changes the equilibrium structure and can affect the mass a star can support, its radius and compactness, and consequently

its surface redshift and tidal response. Anisotropy also influences how the star responds to perturbations: it can change the oscillation frequencies and the point at which radial instability sets in. The size and direction of these changes depend on the assumed anisotropy and, for oscillations and stability, on how the stresses respond when the fluid is perturbed [22, 23, 47–49].

Allowing the radial and tangential pressures to differ introduces an extra unknown into the stellar structure equations. Einstein's equations must therefore be supplemented by a relation that specifies the anisotropy or otherwise connects the matter variables. Several analytical techniques have been developed for this purpose, including prescribed metric potentials, generating functions, symmetry conditions, complexity constraints, and phenomenological relations among the thermodynamic variables [50–55]. Among these approaches, gravitational decoupling (GD) [55] has emerged as a systematic framework for introducing additional matter contributions into known stellar solutions.

From a technical point of view, the anisotropic configurations considered in this work are constructed through GD in its minimal geometric deformation formulation (MGD) [56]. This framework separates the total matter distribution into a known seed source and an additional sector responsible for deforming the original geometry, thereby allowing anisotropic extensions of well-behaved relativistic solutions to be obtained in a controlled manner [55–58]. The method has been widely applied to compact objects containing perfect fluids, polytropic matter, electromagnetic fields, scalar sources, and other effective matter distributions [59–68]. Nevertheless, compliance with regularity, energy, causality, and matching conditions does not guarantee dynamical stability, since an apparently acceptable equilibrium configuration may become unstable under small perturbations.

For this reason, the present study complements the gravitational decoupling construction with an analysis of radial pulsations. The relativistic theory developed by Chandrasekhar describes these oscillations through a discrete spectrum of normal modes, with the fundamental frequency determining the onset of instability [69–73]. Radial oscillations of self-bound quark stars have previously been studied for the MIT bag model, color-superconducting matter, perturbative quantum chromodynamics, and multicomponent configurations [21, 74–76]. In anisotropic systems, however, the difference between radial and tangential stresses modifies both the equilibrium structure and the restoring forces, potentially shifting the maximum stable mass and the point at which the fundamental mode vanishes [22, 23, 48, 49, 77]. Accordingly, the present work investigates self-bound anisotropic stars governed by a generalized linear EoS, with the aim of determining how gravitationally induced anisotropy affects their equilibrium properties, radial oscillation spectrum, and dynamically stable domain.

The paper is organized as follows. Section 2 introduces the relativistic stellar framework and the effective matter variables. Section 3 presents the generalized self-bound EoS, while Section 4 outlines the gravitational decoupling procedure used to construct the anisotropic configurations. Section 5 examines their physical properties and matching conditions. The radial pulsation formalism and stability analysis are developed in Section 6. The main conclusions are summarized in Section 7.

2 Einstein's field equations for an anisotropic relativistic fluid

We consider a static and spherically symmetric self-gravitating configuration described by Einstein's field equations (EFEs),

$$G^{\mu}_{\ \nu} = \frac{8\pi G}{c^4}\, T^{\mu}_{\ \nu}, \tag{1}$$

where $T^{\mu}_{\ \nu} \neq 0$ and represents the energy–momentum tensor associated with the matter distribution. Throughout the remainder of this work, geometrized units $G = c = 1$ are adopted. The interior spacetime is represented by the line element

$$ds^2 = e^{\nu(r)}dt^2 - e^{\lambda(r)}dr^2 - r^2 d\Omega^2, \tag{2}$$

where

$$d\Omega^2 = d\theta^2 + \sin^2\theta\, d\phi^2, \tag{3}$$

and the metric potentials $\nu(r)$ and $\lambda(r)$ depend only on the radial coordinate.

The matter sector is modelled as an anisotropic fluid whose energy–momentum tensor is written as

$$T_{\mu\nu} = (\rho + P_\perp)\, u_\mu u_\nu - P_\perp g_{\mu\nu} + (P_r - P_\perp)\, s_\mu s_\nu, \tag{4}$$

where ρ denotes the energy density, while P_r and $P_\perp$ represent the radial and tangential pressures, respectively. For a comoving observer, the four-velocity and the unit radial vector are given by

$$u^\mu = \left(e^{-\nu/2}, 0, 0, 0\right), \tag{5}$$

and

$$s^\mu = \left(0, e^{-\lambda/2}, 0, 0\right), \tag{6}$$

which satisfy

$$u^\mu u_\mu = 1, \qquad s^\mu s_\mu = -1, \qquad u^\mu s_\mu = 0. \tag{7}$$

Substituting Eqs. (2) and (4) into Eq. (1) yields the independent field equations

$$8\pi\rho = \frac{1-e^{-\lambda}}{r^2} + \frac{e^{-\lambda}\lambda'}{r}, \tag{8}$$

$$8\pi P_r = -\frac{1-e^{-\lambda}}{r^2} + \frac{e^{-\lambda}\nu'}{r}, \tag{9}$$

$$8\pi P_\perp = \frac{e^{-\lambda}}{4}\left[2\nu'' + \nu'^2 - \lambda'\nu' + \frac{2(\nu'-\lambda')}{r}\right], \tag{10}$$

where primes denote derivatives with respect to r.

In an anisotropic configuration, the radial pressure differs from the angular components,

$$P_r(r) \neq P_\theta(r) = P_\phi(r) \equiv P_\perp(r), \tag{11}$$

where the equality between the two angular pressures follows directly from spherical symmetry [47]. It is therefore convenient to introduce the anisotropy factor

$$\Delta(r) = P_\perp(r) - P_r(r). \tag{12}$$

The isotropic limit is recovered when $\Delta = 0$.

The conservation of the energy–momentum tensor follows from the contracted Bianchi identities,

$$\nabla_\mu T^{\mu\nu} = 0, \tag{13}$$

and leads to the generalized Tolman–Oppenheimer–Volkoff equation

$$P_r' = -\frac{\nu'}{2}(\rho + P_r) + \frac{2}{r}(P_\perp - P_r). \tag{14}$$

This expression describes the local equilibrium among the pressure gradient, the gravitational contribution, and the force generated by pressure anisotropy.

Introducing the mass function $m(r)$ through

$$e^{-\lambda(r)} = 1 - \frac{2m(r)}{r}, \tag{15}$$

the first field equation gives

$$\frac{dm}{dr} = 4\pi r^2 \rho. \tag{16}$$

The temporal metric potential can then be expressed as

$$\nu' = 2\frac{m + 4\pi r^3 P_r}{r(r-2m)}. \tag{17}$$

Consequently, Eq. (14) becomes

$$P_r' = -\frac{m + 4\pi r^3 P_r}{r(r-2m)}(\rho + P_r) + \frac{2\Delta}{r}. \tag{18}$$

Equation (18), together with Eq. (16), governs the hydrostatic equilibrium of the anisotropic configuration.

At the center of the star, regularity requires

$$m(0) = 0, \qquad \rho(0) = \rho_c, \qquad P_r(0) = P_\perp(0), \tag{19}$$

where ρ_c denotes the central energy density. The last condition implies that the anisotropy must vanish at the center.

The interior geometry is matched at the stellar surface $r = R \equiv r_\Sigma$ to the exterior Schwarzschild spacetime [78, 79],

$$ds^2 = \left(1 - \frac{2M}{r}\right)dt^2 - \left(1 - \frac{2M}{r}\right)^{-1} dr^2 - r^2 d\Omega^2, \tag{20}$$

where $M = m(R)$ is the total gravitational mass. In the absence of a thin shell at the boundary, continuity of the first and second fundamental forms leads to

$$e^{\nu(R)} = 1 - \frac{2M}{R}, \tag{21}$$

$$e^{-\lambda(R)} = 1 - \frac{2M}{R}, \tag{22}$$

$$P_r(R) = 0. \tag{23}$$

The condition $P_r(R) = 0$ determines the stellar radius during the numerical integration, whereas Eq. (16) gives $m(R) = M$. Notice that the vanishing of the radial pressure does not necessarily imply a vanishing surface density. In particular, self-bound compact stars may satisfy

$$\rho(R) = \rho_s \neq 0, \tag{24}$$

where ρ_s is the finite energy density at zero pressure.

The field equations presented above involve the metric potentials and the thermodynamic variables ρ, P_r, and $P_\perp$, and therefore require additional physical relations to form a closed system. In the next section, this closure is provided by a generalized linear equation of state appropriate for self-bound compact matter. Later, within the gravitational decoupling framework, these quantities will be interpreted as the corresponding effective density and pressures of the complete anisotropic configuration.

3 Generalized linear equation of state for self-bound matter

The equation of state constitutes the fundamental link between the microscopic properties of dense matter and the macroscopic structure of a compact star. In the case of strange quark matter, its precise form remains uncertain because the densities reached in stellar interiors lie in a regime where nonperturbative strong-interaction

effects, the finite strange-quark mass, quark pairing, and possible color-superconducting phases may become relevant [3, 7, 28, 80]. Consequently, phenomenological parametrizations that retain the essential thermodynamic features of self-bound matter provide a useful alternative to model-dependent microscopic descriptions.

A characteristic property of self-bound matter is that its pressure may vanish at a finite energy density. This behaviour distinguishes strange quark stars from conventional gravitationally bound neutron stars and follows naturally from bag-like descriptions of deconfined quark matter [24, 25, 27, 28]. Moreover, detailed MIT bag calculations including a finite strange-quark mass and strong-interaction corrections can be accurately represented, over the range of densities relevant to compact stars, by a linear relation between pressure and energy density [37, 81]. Similar constant-speed-of-sound parametrizations have also been extensively employed in model-independent studies of quark and hybrid stellar matter [31, 38].

Motivated by these considerations, we adopt the generalized linear equation of state

$$P_r = \eta\,(\rho - \rho_s)\,, \qquad 0 < \eta \leq 1, \qquad \rho \geq \rho_s, \tag{25}$$

where P_r is the radial pressure, and ρ denotes the energy density, η is a dimensionless stiffness parameter, and ρ_s represents the energy density at zero pressure. In the present work, ρ must be understood as an energy density rather than a rest-mass density. Equation (25) may equivalently be written as

$$\rho = \rho_s + \frac{P_r}{\eta}. \tag{26}$$

This form belongs to the constant-speed-of-sound class of equations of state and separates two physically different effects: η controls the response of the pressure to compression, whereas ρ_s determines the density scale at which the pressure vanishes [31, 37, 38].

For a stellar configuration with central density ρ_c, the central radial pressure is

$$P_c = \eta\,(\rho_c - \rho_s)\,, \qquad \rho_c > \rho_s. \tag{27}$$

At the stellar surface $r = R$, the condition $P_r(R) = 0$ leads directly to

$$\rho(R) = \rho_s. \tag{28}$$

Therefore, configurations with $\rho_s > 0$ possess a sharp surface with a finite energy density and are self-bound. By contrast, when $\rho_s = 0$, the density also vanishes at the zero-pressure surface, and the corresponding relation does not describe self-bound matter in the strict sense [7, 24, 25].

The radial speed of sound follows immediately from Eq. (25),

$$v_{s,r}^2 = \frac{dP_r}{d\rho} = \eta. \tag{29}$$

In geometrized units, causality requires $v_{s,r}^2 \leq 1$, while local mechanical stability requires $v_{s,r}^2 > 0$. These requirements justify the interval

$$0 < \eta \leq 1. \tag{30}$$

The upper value corresponds to propagation at the speed of light and therefore represents the maximally stiff causal limit rather than a generic microscopic prediction [6, 82, 83]. The frequently used value $\eta = 1/3$, on the other hand, is associated with an ultrarelativistic gas of noninteracting massless particles and should not be interpreted as a universal upper bound for dense matter.

For $\rho_s \geq 0$ and $0 < \eta \leq 1$, the radial pressure automatically satisfies

$$P_r \geq 0, \qquad \rho - P_r = (1-\eta)\rho + \eta\rho_s \geq 0, \tag{31}$$

throughout the stellar interior. Hence, the radial sector is compatible with the inequalities $0 \leq P_r \leq \rho$. Nevertheless, the corresponding conditions for the tangential pressure are not fixed by the radial equation of state and must be verified after constructing the complete anisotropic solution.

Another quantity of particular relevance for the radial-pulsation analysis is the relativistic adiabatic index,

$$\Gamma_r = \frac{\rho + P_r}{P_r}\frac{dP_r}{d\rho}. \tag{32}$$

Using Eq. (25), it becomes

$$\Gamma_r = \eta\frac{\rho + P_r}{P_r} = 1 + \eta + \frac{\rho_s}{\rho - \rho_s}. \tag{33}$$

Although Γ_r diverges formally when $P_r \to 0$ at the surface of a self-bound star, the combination that enters the pulsation equations remains finite,

$$\Gamma_r P_r = \eta\,(\rho + P_r)\,. \tag{34}$$

This property must be taken into account when imposing the surface boundary condition in the radial-stability problem [21, 69, 71, 76].

The generalized relation (25) contains several physically relevant limiting cases, which are discussed below.

3.1 MIT bag-model limit.

In the simplest MIT bag description, cold quark matter is composed of noninteracting and massless up, down, and strange quarks confined by a vacuum energy density B [28, 36]. For the quark contribution,

$$\rho_q = 3P_q, \tag{35}$$

while the bag vacuum modifies the total energy density and pressure according to

$$\rho = \rho_q + B, \qquad P_r = P_q - B. \tag{36}$$

The opposite signs of the vacuum contribution follow from its thermodynamic interpretation. The bag constant $B > 0$ represents the excess vacuum energy density inside the bag relative to the exterior vacuum. For a volume V, the corresponding energy is $E_{\rm vac} = BV$. Since B is constant, its pressure contribution is

$$P_{\rm vac} = -\frac{\partial E_{\rm vac}}{\partial V} = -B. \tag{37}$$

Thus, the bag vacuum increases the total energy density while reducing the pressure, reflecting the energy cost of expanding the region occupied by deconfined quark matter. Both contributions are dimensionally consistent, since pressure and energy density have the same physical dimensions.

Eliminating the quark variables gives

$$P_r = \frac{1}{3}\left(\rho - 4B\right). \tag{38}$$

Therefore, the simplest MIT bag radial relation is recovered from the generalized linear equation of state by choosing

$$\eta = \frac{1}{3}, \qquad \rho_s = 4B. \tag{39}$$

The finite value $\rho(R) = 4B$ reflects the self-bound character of the radial relation. In an anisotropic configuration, this identification does not by itself recover the complete stress tensor of an isotropic MIT bag fluid; the tangential stress requires a separate prescription. Finite quark masses, perturbative strong-interaction corrections, and pairing effects modify this simple relation, but their resulting equations of state can frequently be approximated by the same linear form with effective values of η and ρ_s [28, 37, 38, 80].

3.2 Conformal ultrarelativistic limit.

For $\eta = \frac{1}{3}$ and $\rho_s = 0$, the EoS becomes

$$P_r = \frac{\rho}{3}. \tag{40}$$

This reproduces the radial pressure–energy-density relation of an ideal conformal gas of massless particles. For the complete anisotropic fluid, however, $T^{\mu}{}_{\mu} = \rho - P_r - 2P_\perp = -2\Delta$ when $P_r = \rho/3$, so a vanishing trace additionally requires $\Delta = 0$. A relation between radial pressure and density is not enough to establish whether the full matter sector is conformal, since the tangential stresses also enter the trace of the energy–momentum tensor. The absence of a vacuum offset has a separate consequence: the density vanishes when the radial pressure reaches zero. Thus, although Eqs. (38) and (40) give the same radial sound speed, they describe different surface behaviour. The MIT bag relation allows a finite density at zero pressure, as required for self-bound matter, whereas the relation without an offset does not.

3.3 Zel'dovich stiff-fluid limit.

The choice $\eta = 1$ and $\rho_s = 0$, reduces Eq. (25) to the Zel'dovich equation of state,

$$P_r = \rho. \tag{41}$$

This relation describes the most rigid fluid compatible with relativistic causality, since $dP_r/d\rho = 1$ [82,83]. It is useful as a limiting case for estimating the largest pressure support allowed by causality. Nevertheless, because the density vanishes when the pressure vanishes, the unshifted Zel'dovich relation is not a self-bound equation of state.

3.4 Causal self-bound limit.

A self-bound generalization of the maximally stiff case is obtained by setting

$$\eta = 1, \qquad \rho_s > 0, \tag{42}$$

which yields

$$P_r = \rho - \rho_s. \tag{43}$$

This equation preserves the causal-limit sound speed while allowing the pressure to vanish at the finite density ρ_s. It may therefore be viewed as a shifted Zel'dovich relation or as the maximally stiff member of the self-bound family. The distinction between Eqs. (41)

and (43) will be important when comparing gravitationally bound and self-bound configurations.

More generally, the choices

$$0 < \eta < 1, \qquad \rho_s > 0, \tag{44}$$

describe a continuous family of causal self-bound equations of state. By varying η, one may investigate how the stiffness of dense matter affects the stellar mass, radius, compactness, and radial oscillation spectrum, while ρ_s independently controls the density scale associated with the stellar surface. This separation is one of the principal advantages of the generalized linear parametrization.

It should be emphasized that Eq. (25) constrains only the radial thermodynamic sector. It does not prescribe the tangential pressure or the anisotropy factor. In the present model, these quantities will be generated by the additional gravitational source introduced through the minimal geometric deformation method. Thus, in the following section, the generalized linear equation of state will be imposed on the effective radial pressure and energy density of the complete gravitationally decoupled configuration, providing the closure relation required to determine the geometric deformation.

4 Gravitational decoupling through minimal geometric deformation

In this section, we introduce the GD framework through the MGD approach [55–58]. In this method the energy–momentum tensor that appears in EFEs decomposes into a known seed gravitational source and an additional matter sector,

$$T_{\mu\nu} = \widehat{T}_{\mu\nu} + \Theta_{\mu\nu}, \tag{45}$$

where $\widehat{T}_{\mu\nu}$ describes the seed configuration and $\Theta_{\mu\nu}$ represents the effective source responsible for the deformation of the original geometry. In the present formulation, the usual coupling parameter is absorbed into the additional source and into the geometric deformation. Thus, $\Theta_{\mu\nu}$ and the deformation function introduced below represent the complete physical contribution of the decoupling sector.

The seed source is usually assumed to correspond to an isotropic perfect fluid,

$$\widehat{T}^{\mu}_{\ \nu} = \mathrm{diag}\left(\widehat{\rho}, -\widehat{P}, -\widehat{P}, -\widehat{P}\right), \tag{46}$$

where $\widehat{\rho}$ and $\widehat{P}$ denote the seed density and pressure, respectively. The effective variables associated with the additional source are defined as

$$\rho_\Theta = \Theta^0_{\ 0}, \qquad P_r^\Theta = -\Theta^1_{\ 1}, \qquad P_\perp^\Theta = -\Theta^2_{\ 2}. \tag{47}$$

Consequently, the density and pressures of the complete configuration are

$$\rho = \widehat{\rho} + \rho_\Theta, \tag{48}$$

$$P_r = \widehat{P} + P_r^\Theta, \tag{49}$$

$$P_\perp = \widehat{P} + P_\perp^\Theta. \tag{50}$$

Since the seed sector is isotropic, the anisotropy of the total configuration is generated entirely by the additional source,

$$\Delta = P_\perp - P_r = P_\perp^\Theta - P_r^\Theta. \tag{51}$$

Within the standard MGD prescription, the temporal metric potential is kept unchanged, while the radial metric component is deformed. Accordingly, the radial metric potential is written as

$$e^{-\lambda(r)} = \mu(r) + \mathcal{F}(r), \tag{52}$$

where $\mu(r)$ belongs to the isotropic seed geometry and $\mathcal{F}(r)$ denotes the physical geometric deformation induced by the additional source. The complete interior line element therefore becomes

$$ds^2 = e^{\nu(r)}dt^2 - \frac{dr^2}{\mu(r) + \mathcal{F}(r)} - r^2 d\Omega^2. \tag{53}$$

The seed solution is recovered in the limit $\mathcal{F}(r) \to 0$.

Substitution of Eq. (52) into Einstein's field equations separates the system into two sets. The first set corresponds to the isotropic seed sector,

$$8\pi\widehat{\rho} = \frac{1-\mu}{r^2} - \frac{\mu'}{r}, \tag{54}$$

$$8\pi\widehat{P} = -\frac{1}{r^2} + \mu\left(\frac{1}{r^2} + \frac{\nu'}{r}\right), \tag{55}$$

$$8\pi\widehat{P} = \frac{\mu}{4}\left(2\nu'' + \nu'^2 + \frac{2\nu'}{r}\right) + \frac{\mu'}{4}\left(\nu' + \frac{2}{r}\right). \tag{56}$$

The equality between the last two equations expresses the isotropic character of the seed fluid. Once a particular perfect-fluid solution is selected, the functions $\{\nu, \mu, \widehat{\rho}, \widehat{P}\}$ are completely determined. In the following section, the Tolman IV solution will be adopted as the isotropic seed.

The second set governs the effective decoupling source,

$$8\pi\rho_\Theta = -\left(\frac{\mathcal{F}}{r^2} + \frac{\mathcal{F}'}{r}\right), \tag{57}$$

$$8\pi P_r^\Theta = \mathcal{F}\left(\frac{1}{r^2} + \frac{\nu'}{r}\right), \tag{58}$$

$$8\pi P_\perp^\Theta = \frac{\mathcal{F}}{4}\left(2\nu'' + \nu'^2 + \frac{2\nu'}{r}\right) + \frac{\mathcal{F}'}{4}\left(\nu' + \frac{2}{r}\right). \tag{59}$$

These relations show that the density and both pressure components of the additional source are completely determined once the deformation $\mathcal{F}(r)$ is known.

The total physical variables may therefore be written directly as

$$8\pi\rho = 8\pi\widehat{\rho} - \left(\frac{\mathcal{F}}{r^2} + \frac{\mathcal{F}'}{r}\right), \tag{60}$$

$$8\pi P_r = 8\pi\widehat{P} + \mathcal{F}\left(\frac{1}{r^2} + \frac{\nu'}{r}\right), \tag{61}$$

$$8\pi P_\perp = 8\pi\widehat{P} + \frac{\mathcal{F}}{4}\left(2\nu'' + \nu'^2 + \frac{2\nu'}{r}\right) + \frac{\mathcal{F}'}{4}\left(\nu' + \frac{2}{r}\right). \tag{62}$$

Equations (60) and (62) make explicit that the complete anisotropic matter distribution can be obtained directly from the seed solution and the geometric deformation.

The mass function is also modified by the decoupling sector. Introducing the seed mass function through

$$\mu(r) = 1 - \frac{2\widehat{m}(r)}{r}, \tag{63}$$

and comparing Eq. (52) with

$$e^{-\lambda(r)} = 1 - \frac{2m(r)}{r}, \tag{64}$$

one obtains

$$m(r) = \widehat{m}(r) - \frac{r}{2}\mathcal{F}(r). \tag{65}$$

Thus, the deformation modifies both the local mass distribution and the total gravitational mass of the star.

The contracted Bianchi identities ensure the conservation of the complete energy–momentum tensor. Under the standard MGD assumption that the two sectors exchange no energy–momentum except through their common gravitational field, they may be treated as separately conserved. The seed perfect fluid satisfies

$$\widehat{P}' + \frac{\nu'}{2}\left(\widehat{\rho} + \widehat{P}\right) = 0, \tag{66}$$

whereas the additional source obeys

$$\left(P_r^{\Theta}\right)' + \frac{\nu'}{2}\left(\rho_\Theta + P_r^{\Theta}\right) - \frac{2}{r}\left(P_\perp^{\Theta} - P_r^{\Theta}\right) = 0. \tag{67}$$

The latter relation is not an independent field equation, since it follows from Equations (57) and (59).

4.1 Closure of the gravitationally decoupled system

Once the isotropic seed is selected, the functions ν, μ, $\widehat{\rho}$, and $\widehat{P}$ are known. The remaining unknown functions may be expressed as

$$\{\mathcal{F},\, \rho,\, P_r,\, P_\perp\}, \tag{68}$$

or, equivalently, in terms of the decoupling sector as

$$\left\{\mathcal{F},\, \rho_\Theta,\, P_r^{\Theta},\, P_\perp^{\Theta}\right\}. \tag{69}$$

EFEs provide three independent relations, Eqs. (57) and (59), for these four unknown functions. Therefore, one additional physical condition is required to close the system.

In the present work, closure is achieved by imposing the generalized linear equation of state introduced in Section 3 on the total effective density and radial pressure,

$$P_r = \eta\,(\rho - \rho_s). \tag{70}$$

Using Eqs. (60) and (61), this condition becomes

$$\widehat{P} + \frac{\mathcal{F}}{8\pi}\left(\frac{1}{r^2} + \frac{\nu'}{r}\right) = \eta\left[\widehat{\rho} - \rho_s - \frac{1}{8\pi}\left(\frac{\mathcal{F}}{r^2} + \frac{\mathcal{F}'}{r}\right)\right]. \tag{71}$$

It follows that the geometric deformation satisfies the first-order differential equation

$$\mathcal{F}' + \left[\frac{\nu'}{\eta} + \frac{1+\eta}{\eta r}\right]\mathcal{F} = \frac{8\pi r}{\eta}\left[\eta\,(\widehat{\rho} - \rho_s) - \widehat{P}\right]. \tag{72}$$

All coefficients in this equation are known once the isotropic seed and the EoS parameters η and ρ_s have been specified. Regularity at the center requires

$$\mathcal{F}(r) = \mathcal{O}(r^2) \qquad \text{as} \qquad r \to 0. \tag{73}$$

Solving Eq. (72) determines $\mathcal{F}(r)$. The final density, radial pressure, and tangential pressure then follow directly from Eqs. (60) and (62).

Therefore, once the Tolman IV geometry [50] is adopted as the isotropic seed, the metric potentials and the corresponding seed density and pressure are known up to the constants characterizing the solution. The remaining functional freedom of the gravitationally decoupled configuration is encoded in the geometric deformation $\mathcal{F}(r)$. The three quasi-Einstein equations express the density, radial pressure, and tangential pressure of the additional sector in terms of this deformation, while the generalized linear equation of state, imposed on the total effective density and radial pressure, supplies the independent physical relation

required for closure. The resulting first-order differential equation for $\mathcal{F}(r)$ therefore constitutes the central structure equation of the present construction.

This closure does not, however, complete the stellar problem by itself. The deformation equation must be solved subject to central regularity, after which the total density and pressure profiles are reconstructed from the EFEs. The stellar surface is subsequently determined by the vanishing of the radial pressure, and the constants of the Tolman IV seed are constrained by the matching conditions with the exterior Schwarzschild geometry. The resulting configurations must finally be examined for physical acceptability and dynamical stability. Thus, once the Tolman IV temporal potential has been chosen, the total-fluid radial EoS closes the remaining deformation problem without prescribing an additional anisotropy profile. The choice of temporal potential remains an essential geometric assumption of the construction.

5 Anisotropic self-bound strange-star configurations

We specialize the construction of Section 4 to the Tolman IV temporal potential and impose the generalized linear EoS on the complete matter distribution. The resulting solution can be written in closed form for the four stiffness values $\eta = 1, 1/2, 1/3, 1/4$. For each stiffness we retain three compactness values and resolve the dependence of the metric, matter variables, and profile diagnostics on compactness. Constant radial-sound-speed profiles are omitted; the constant $\rho - P_r$ figure is also omitted for $\eta = 1$. The surface density is fixed by regularity and Schwarzschild matching once the compactness and length scale are specified. This construction provides the equilibrium backgrounds for the explicitly closed radial-perturbation problem studied in Section 6.

5.1 Geometry and dimensionless variables

Let

$$x = \frac{r}{R}, \quad u = \frac{M}{R}, \quad a = 1 - 3u, \quad b(x) = a + ux^2. \tag{74}$$

The temporal potential takes the form

$$e^{\nu(r)} = b(x) = 1 - 3u + ux^2. \tag{75}$$

At the surface, the temporal metric potential satisfies $e^{\nu(R)} = 1 - 2u$. Keeping it positive and nonsingular throughout the interior restricts the compactness to $0 < u < 1/3$. This condition ensures regularity of the temporal potential, but the matter variables and stability must still be examined before the configuration can be considered physically acceptable.

A convenient Tolman IV seed with this temporal potential is [50]

$$\mu(x) = \frac{(1 - ux^2)b(x)}{a + 2ux^2}. \tag{76}$$

In the conventional parametrization $e^{\nu} = B^2(1 + r^2/A^2)$, this corresponds to $A^2/R^2 = a/u$, $B^2 = a$, and $C^2/R^2 = 1/u$. We denote the complete radial potential by

$$H(x) = e^{-\lambda(r)} = \mu(x) + \mathcal{F}(x). \tag{77}$$

The seed choice fixes the decomposition into μ and $\mathcal{F}$; the total potential H will be determined directly by the total-fluid EoS. No additional seed-shape parameter is needed for this matched family.

Introduce the dimensionless matter variables

$$\begin{aligned} &\varepsilon = 8\pi R^2 \rho, \quad p = 8\pi R^2 P_r, \\ &t = 8\pi R^2 P_\perp, \quad s = 8\pi R^2 \rho_s. \end{aligned} \tag{78}$$

Here s is constant within each star and the EoS becomes $p = \eta(\varepsilon - s)$. With $H_x = dH/dx$, Einstein's equations give

$$\varepsilon = \frac{1 - H}{x^2} - \frac{H_x}{x}, \tag{79}$$

$$p = \frac{H - 1}{x^2} + \frac{2uH}{b}, \tag{80}$$

$$t = \frac{u(2a + ux^2)H}{b^2} + \frac{a + 2ux^2}{2xb} H_x. \tag{81}$$

The apparent divisions by x are evaluated by their regular limits at the center. The dimensionless anisotropy is $\delta = t - p = 8\pi R^2 \Delta$.

5.2 Exact closure and surface matching

Substituting Eqs. (79) and (80) into the EoS yields

$$\eta x H_x + \left(1 + \eta + \frac{2ux^2}{b}\right) H = 1 + \eta - \eta s x^2. \tag{82}$$

This is equivalent to the deformation equation of Section 4, with $\mathcal{F} = H - \mu$. Set $n = 1/\eta$ and define

$$I_j(x) = \int_0^x y^{n+j} b(y)^n \, dy, \qquad j = 0, 2. \tag{83}$$

The regular solution is

$$H(x) = \frac{(n + 1)I_0(x) - sI_2(x)}{x^{n+1} b(x)^n}. \tag{84}$$

The omitted homogeneous term is proportional to $x^{-(n+1)}b^{-n}$ and is singular at the center. Thus regularity removes its integration constant.

At $x = 1$, Schwarzschild matching requires $H(1) = 1 - 2u$. Equation (80) then gives $p(1) = 0$, and the EoS gives $\varepsilon(1) = s$. Consequently,

$$s = \frac{(n+1)I_0(1) - (1-2u)^{n+1}}{I_2(1)}. \tag{85}$$

The interior density consequently approaches a finite value $\rho(R^-) = \rho_s > 0$, whereas the exterior Schwarzschild region has $\rho(R^+) = 0$. This finite surface-density jump is the self-bound boundary assumed here. The surface is defined by vanishing radial pressure, not by vanishing density. In particular, for $\eta = 1$ one has $\rho = P_r + \rho_s$, so a nonzero endpoint of the density profile at $x = 1$ is required by the EoS rather than a failure of the matching conditions.

The quantities u, R, and ρ_s are therefore not independent. For a chosen positive physical surface density,

$$R = \sqrt{\frac{s(u,\eta)}{8\pi\rho_s}}, \qquad M = uR. \tag{86}$$

This scaling is essential when interpreting a sequence at fixed EoS: setting $R = 1$ is a dimensionless plotting convention, not a common dimensional radius for all stars at fixed ρ_s.

For the four cases considered here, $n = 1, 2, 3, 4$ is an integer. Define the finite polynomials

$$L_j(x) = \sum_{k=0}^{n} \binom{n}{k} \frac{a^{n-k}u^k x^{2k}}{n+j+2k+1}, \qquad j = 0, 2. \tag{87}$$

Since $I_j = x^{n+j+1}L_j$, the closed solution is simply

$$H(x) = \frac{(n+1)L_0(x) - sx^2L_2(x)}{b(x)^n}, \tag{88}$$

$$s = \frac{(n+1)L_0(1) - (1-2u)^{n+1}}{L_2(1)}. \tag{89}$$

These expressions specify all four families without long expanded rational functions or numerical integration constants. For example, at $\eta = 1$,

$$s = \frac{6u(3-8u)}{3-7u},$$
$$H = \frac{a + (u/2 - sa/4)x^2 - (su/6)x^4}{b}. \tag{90}$$

The existence of this formal solution does not ensure that it passes the additional matter diagnostics discussed below.

Table 1 Compactness values used for the equilibrium profiles and radial pulsations. All profile curves are solid; blue, orange, and green denote u_1, u_2, and u_3, respectively.

η	u_1	u_2	u_3
1	0.100	0.148	0.196
1/2	0.227	0.243	0.259
1/3	0.181	0.213	0.244
1/4	0.158	0.200	0.241

5.3 Profile definitions and compactness sets

The configuration sets are listed in Table 1. For each stiffness, nine profiles are grouped into a multipanel figure: $e^{-\lambda}$, ρ, P_r, P_t, Δ, $\rho - P_t$, $\rho - P_r - 2P_t$, v_t, and ρ''. The quantity $\rho - P_r$ is not plotted, since its nonnegativity follows directly from Eq. (31); for $\eta = 1$ it is also constant. Here $P_t \equiv P_\perp$, $\Delta = P_t - P_r$, and primes denote derivatives with respect to the areal radius r. All three compactness values in a row of the table are used in every equilibrium-profile panel for that family.

To retain a direct comparison with the dimensionless convention $R = 1$, the matter profiles display $R^2\rho$, R^2P_r, R^2P_t, and the corresponding stress combinations, rather than normalizing each curve by a different surface density. In terms of Eqs. (79) and (81), these are $\varepsilon/(8\pi)$, $p/(8\pi)$, and $t/(8\pi)$. The curvature figure displays

$$R^4\rho''(r) = \frac{1}{8\pi}\frac{d^2\varepsilon}{dx^2}. \tag{91}$$

Thus the factors of R restore the dimensions suppressed by setting $R = 1$. The different curves do not assume a common dimensional radius at fixed ρ_s; such a physical sequence must use Eq. (86).

The common temporal potential and redshift are shown separately in Figs. 1 and 2 for $u = 0.100, 0.180, 0.259$. Their expressions are independent of η and remain unchanged when the total-fluid EoS is imposed on the radial potential:

$$e^\nu = b(x), \qquad z(x) = b(x)^{-1/2} - 1. \tag{92}$$

The temporal potential increases outward, while the redshift decreases. Increasing u lowers e^ν and raises z throughout the star, with a larger central-to-surface contrast.

We define the radial sound speed and the plotted tangential-profile diagnostic by

$$v_r = \sqrt{\frac{dP_r}{d\rho}} = \sqrt{\eta},$$
$$v_t = \sqrt{\frac{P_t'}{\rho'}} = \sqrt{\frac{t_x}{\varepsilon_x}}. \tag{93}$$

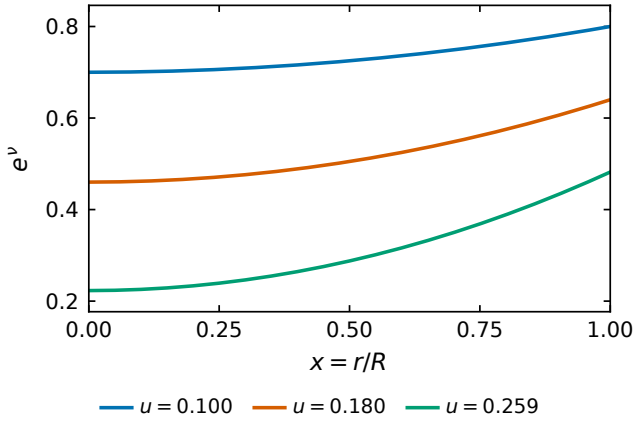


Fig. 1 Temporal potential e^{ν} for $u = 0.100, 0.180, 0.259$. This expression is independent of η.

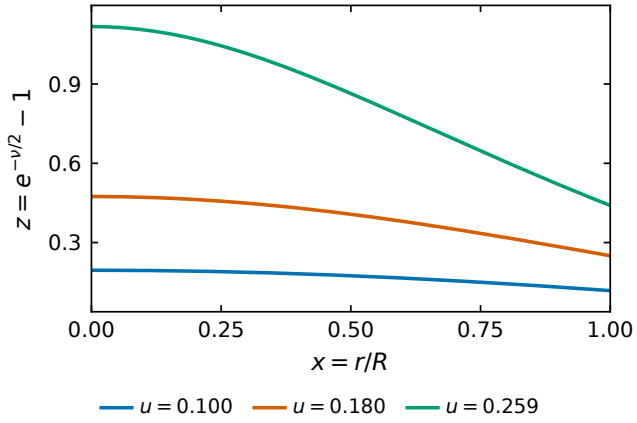


Fig. 2 Gravitational redshift for the same compactness values as Fig. 1.

The radial EoS therefore requires horizontal v_r profiles. At a fixed η the three u curves coincide exactly, so these constant profiles are omitted. The constant value differs between stiffnesses. Radially varying v_r curves would contradict Eq. (25) with constant η and ρ_s. Here, v_t is calculated from the radial gradients of the equilibrium pressure and density. To determine whether it represents a propagation speed, we also need a constitutive law describing how the anisotropic stress responds to perturbations. At the center, the ratio is evaluated by its regular limit,

$$v_t^2(0) = \frac{t_{xx}(0)}{\varepsilon_{xx}(0)} = \frac{15\eta - 1}{10}. \tag{94}$$

The squared tangential ratios are positive for all displayed profiles, so all square roots plotted here are real.

The three stress-combination profiles must also be distinguished. The first two test the upper-pressure inequalities $P_r \le \rho$ and $P_t \le \rho$. When tension is present, the dominant energy condition additionally requires $\rho + P_t \ge 0$; equivalently one must check $\rho \ge |P_t|$. The third combination,

$$\mathcal{T} = \rho - P_r - 2P_t, \tag{95}$$

is a trace combination, not the strong-energy-condition sum. The latter contains $\rho + P_r + 2P_t$, together with $\rho + P_i \ge 0$. A negative $\mathcal{T}$ must therefore not be described as a violation of that energy condition. Likewise, ρ'' measures the curvature of the density profile; its sign alone does not establish dynamical or convective stability.

5.4 The maximally stiff family: $\eta = 1$

Figures 3a–3i show the nine retained profiles for $u = 0.100, 0.148, 0.196$. The radial metric is regular at the center, $H(0) = 1$, and reaches $H(1) = 1 - 2u$. The density and radial pressure decrease outward, with $P_r(R) = 0$ and a finite positive surface density. The central density and pressure grow across the displayed compactness set. The tangential pressure equals the radial pressure at the center and becomes negative in an outer layer: its zero occurs at $x \simeq 0.8413, 0.8388, 0.8359$, respectively. The anisotropy is negative for $0 < x \le 1$, corresponding to an inward anisotropic contribution to hydrostatic balance.

The relation $\rho - P_r = \rho_s$ at $\eta = 1$ is an exact EoS consequence, so its constant figure is omitted. The combinations $\rho - P_t$ and $\mathcal{T}$ remain positive for the displayed configurations. The radial diagnostic is $v_r = 1$, whereas $v_t(0) = \sqrt{7/5} \simeq 1.1832$. In fact, $v_t > 1$ throughout all three displayed interiors. These solutions are therefore retained as formal comparisons and fail the usual subluminal tangential-profile diagnostic; they are not presented as configurations satisfying every physical-acceptability criterion.

The density curvature is negative throughout the $u = 0.100$ profile. For $u = 0.148$ and 0.196 it changes sign at $x \simeq 0.9104$ and 0.6810. These inflection points do not reverse the outward decrease of ρ.

5.5 The intermediate-stiffness family: $\eta = 1/2$

Figures 4a–4i retain $u = 0.227, 0.243, 0.259$. The radial metric remains positive, and the density and both pressures decrease outward. The radial pressure vanishes at the surface, while the tangential pressure crosses zero at $x \simeq 0.9051, 0.9169, 0.9350$ and is negative beyond those radii. The anisotropy is negative away from the center for all three curves. Hence these configurations contain a surface-adjacent region of tangential tension; imposing $P_t \ge 0$ as an additional condition would exclude them.

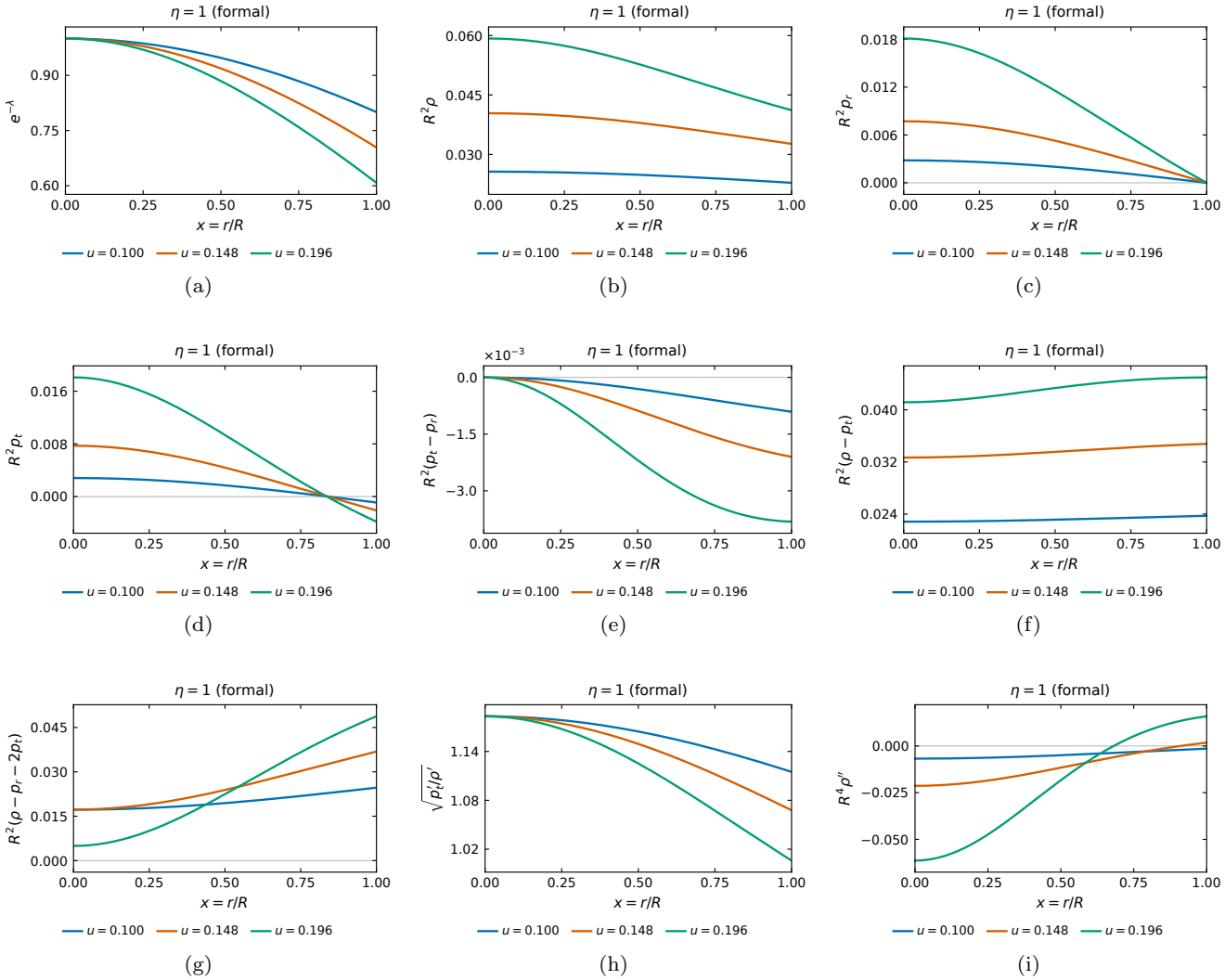


Fig. 3 Equilibrium profiles and diagnostics for $\eta = 1$: (a) radial metric potential $e^{-\lambda}$; (b) density $R^2\rho$, with finite positive surface density; (c) radial pressure $R^2 P_r$, which vanishes at $r = R$; (d) tangential pressure $R^2 P_t$; (e) anisotropy $R^2(P_t - P_r)$; (f) tangential stress combination $R^2(\rho - P_t)$; (g) trace combination $R^2(\rho - P_r - 2P_t)$, which is not the strong-energy-condition sum; (h) tangential-profile diagnostic $v_t = \sqrt{P_t'/\rho'}$; and (i) density curvature $R^4\rho''$, whose sign changes indicate inflection points.

Both $\rho - P_r$ and $\rho - P_t$ remain positive. The trace combination is positive for the first two compactness values, but the $u = 0.259$ configuration has $\mathcal{T} < 0$ in its central region, up to $x \simeq 0.1485$. This is reported explicitly rather than suppressing the curve. The independent energy-condition checks below show why it must not be confused with a violation of the strong energy condition.

The radial velocity is the common constant $v_r = 1/\sqrt{2} \simeq 0.7071$. The tangential diagnostic starts at $\sqrt{13/20} \simeq 0.8062$ and decreases to approximately 0.6462, 0.6331, and 0.6236 at the respective surfaces. The curvature ρ'' changes sign at $x \simeq 0.4971, 0.4428, 0.3891$: the inflection point moves inward as compactness increases, although the density remains monotone.

5.6 The MIT bag radial relation: $\eta = 1/3$

For $\eta = 1/3$, identifying $\rho_s = 4B$ gives $P_r = (\rho - 4B)/3$. Figures 5a–5i use $u = 0.181, 0.213, 0.244$. Again $H > 0$, the density and radial pressure decrease outward, and the radial pressure reaches zero at a nonzero surface density. The first two configurations have small tangential tensions near the surface, beginning at $x \simeq 0.9597$ and 0.9904. At $u = 0.244$, P_t remains positive throughout; the anisotropy changes from negative to positive at

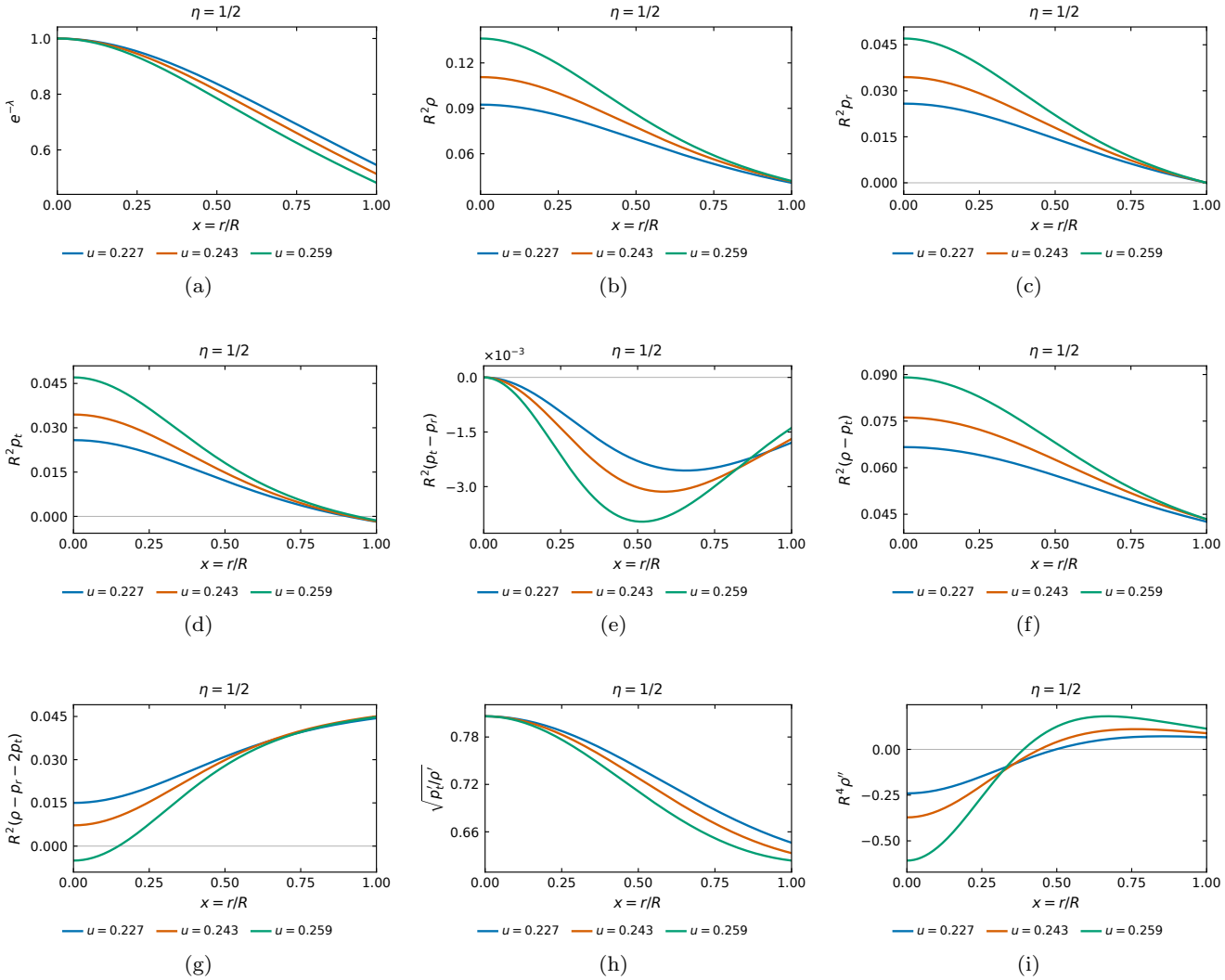


Fig. 4 Equilibrium profiles and diagnostics for $\eta = 1/2$: (a) radial metric potential $e^{-\lambda}$; (b) density $R^2\rho$, with finite positive surface density; (c) radial pressure R^2P_r, which vanishes at $r = R$; (d) tangential pressure R^2P_t; (e) anisotropy $R^2(P_t - P_r)$; (f) tangential stress combination $R^2(\rho - P_t)$; (g) trace combination $R^2(\rho - P_r - 2P_t)$, which is not the strong-energy-condition sum; (h) tangential-profile diagnostic $v_t = \sqrt{P_t'/\rho'}$; and (i) density curvature $R^4\rho''$, whose sign changes indicate inflection points.

$x \simeq 0.8433$. Thus the sign of the anisotropy and the sign of the tangential pressure carry different information.

All three displayed stress combinations are positive. The radial velocity is $v_r = 1/\sqrt{3} \simeq 0.5774$, and the tangential diagnostic starts at $\sqrt{2/5} \simeq 0.6325$ and remains below unity. The density-curvature zeros occur at $x \simeq 0.6191, 0.5073, 0.4084$. If nonnegative tangential pressure and the subluminal profile diagnostics are required simultaneously, only the $u = 0.244$ example among these three passes those particular tests. This statement concerns the sampled configurations and is not a bound on the complete family.

5.7 The softer family: $\eta = 1/4$

Figures 6a–6i use $u = 0.158, 0.200, 0.241$. The radial metric and density are positive, both pressures decrease outward, and P_t stays positive, including at the surface. The anisotropy is initially negative but becomes positive beyond $x \simeq 0.8279, 0.6417, 0.4865$, respectively. A larger compactness therefore moves the change in the anisotropic contribution to smaller fractional radius within this set.

All three configurations have positive values of $\rho - P_r$, $\rho - P_t$, and $\mathcal{T}$, and share the constant radial sound speed $v_r = 1/2$. The tangential diagnostic starts at $\sqrt{11/40} \simeq 0.5244$ at the center, independently of u, and ranges from approximately 0.4526 to 0.5244 across

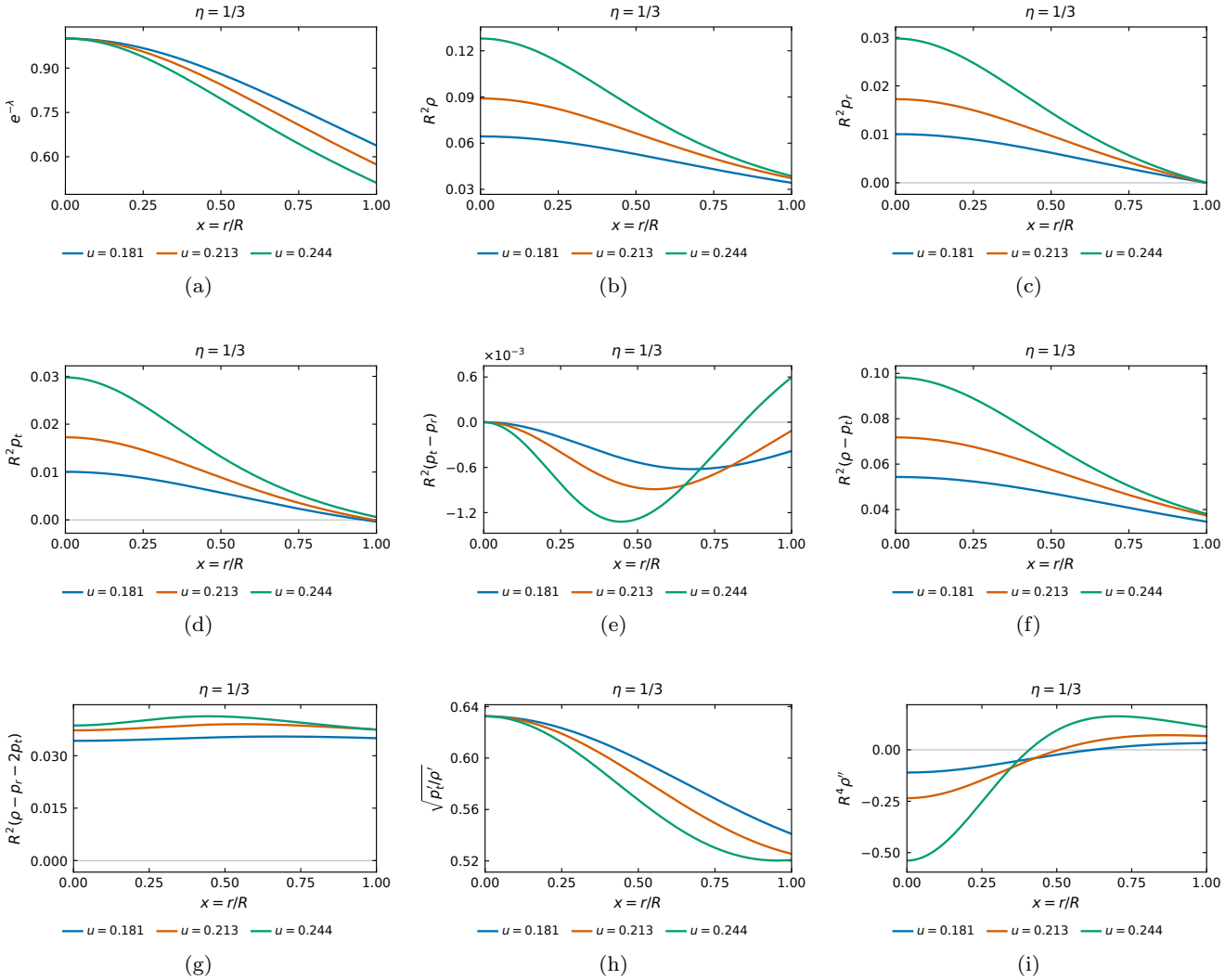


Fig. 5 Equilibrium profiles and diagnostics for $\eta = 1/3$: (a) radial metric potential $e^{-\lambda}$; (b) density $R^2\rho$, with finite positive surface density; (c) radial pressure $R^2 P_r$, which vanishes at $r = R$; (d) tangential pressure $R^2 P_t$; (e) anisotropy $R^2(P_t - P_r)$; (f) tangential stress combination $R^2(\rho - P_t)$; (g) trace combination $R^2(\rho - P_r - 2P_t)$, which is not the strong-energy-condition sum; (h) tangential-profile diagnostic $v_t = \sqrt{P_t'/\rho'}$; and (i) density curvature $R^4\rho''$, whose sign changes indicate inflection points.

the three models. Near the surface, the shape of the v_t profile varies with compactness. In the most compact model ($u = 0.241$), v_t decreases to a minimum before increasing again towards the surface. The density continues to decrease throughout the interior, with $\rho' < 0$ for $0 < x \leq 1$, even though its curvature changes sign at $x \simeq 0.6750, 0.5232, 0.3966$, respectively. The pressures remain nonnegative and the velocity profiles stay below unity in all three cases. These checks support the acceptability of the equilibrium profiles, but dynamical stability requires a separate perturbation analysis.

5.8 Consistency checks and physical scope

All twelve configurations satisfy central isotropy, $P_r(0) = P_t(0)$, and the matching conditions $H(1) = 1 - 2u$, $P_r(R) = 0$, and $\rho(R) = \rho_s$. The conservation equation is the exact identity

$$p_x = -\frac{ux}{b}(\varepsilon + p) + \frac{2(t - p)}{x}. \tag{96}$$

The EoS, matching, central limits, and stress-balance relations were checked algebraically. Independent integration of Eq. (82) agrees with the closed solution to better than 10^{-8} in H for all twelve examples, and integrating the density reproduces $M = uR$.

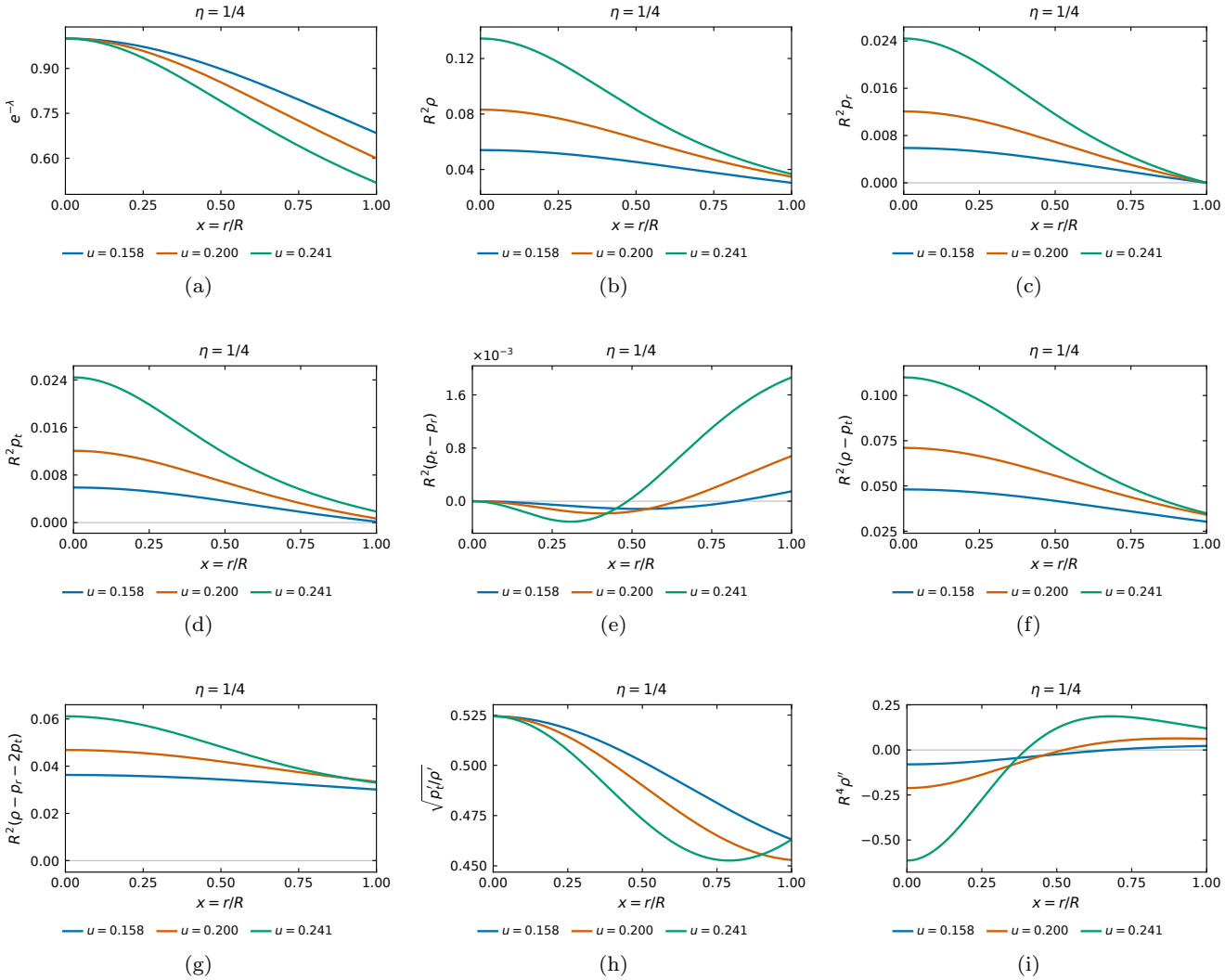


Fig. 6 Equilibrium profiles and diagnostics for $\eta = 1/4$: (a) radial metric potential $e^{-\lambda}$; (b) density $R^2\rho$, with finite positive surface density; (c) radial pressure $R^2 P_r$, which vanishes at $r = R$; (d) tangential pressure $R^2 P_t$; (e) anisotropy $R^2(P_t - P_r)$; (f) tangential stress combination $R^2(\rho - P_t)$; (g) trace combination $R^2(\rho - P_r - 2P_t)$, which is not the strong-energy-condition sum; (h) tangential-profile diagnostic $v_t = \sqrt{P_t'/\rho'}$; and (i) density curvature $R^4\rho''$, whose sign changes indicate inflection points.

Evaluation on 4001 equally spaced points gives $H > 0$, $\rho > 0$, $P_r \geq 0$ (up to numerical roundoff at the surface), and decreasing density and radial pressure in every displayed configuration. The inequalities $\rho \geq |P_r|$, $\rho \geq |P_t|$, $\rho + P_i \geq 0$, and $\rho + P_r + 2P_t \geq 0$ also hold on that grid. These numerical checks apply to the displayed examples and do not establish a global allowed interval of u. In particular, they neither remove the reported tangential tensions nor make the $\eta = 1$ family pass its failed tangential-profile test.

Matching requires $P_r(R) = 0$, but not $P_t(R) = 0$. Tangential tensions occur in phenomenological anisotropic strange-star models [84]. A model that forbids tension must exclude the affected configurations. Self-boundness does not by itself provide a microscopic justification for anisotropic stress.

It should be noted that negative pressure anisotropy, $\Delta < 0$, has previously been considered in relativistic models of neutron stars and quark stars, including studies on non-radial oscillations, radial stability, and f-modes [44, 85, 86]. Pressure anisotropy may arise from condensates, elastic or crystalline phases, and strong magnetic fields; however, its sign depends on the material response and, where relevant, the field geometry. For $\Delta = P_t - P_r < 0$, radial pressure dominates over tangential pressure, and the anisotropic contribution to hydrostatic balance, $2\Delta/r$, points inward. The presence

of this phenomenology does not, in itself, imply dynamical instability within the star.

The equilibrium profiles alone do not establish dynamical stability. Section 6 specifies two constitutive prescriptions for the anisotropy perturbation and solves the associated radial eigenvalue problems. Those conditional stability results do not supply a microscopic origin for the anisotropic stresses or determine a maximum stable mass.

6 Radial pulsations of the self-bound configurations

We now investigate the linear radial response of the twelve equilibrium configurations considered above. A static anisotropy profile does not specify how the anisotropic stress responds to a displacement of the fluid. We therefore state the material response explicitly and compare two closures that reproduce the same equilibrium. The resulting stability statements refer to these closures. This distinction is particularly relevant when the tangential pressure remains nonzero at the surface, as in radial-stability studies of anisotropic strange stars [22].

6.1 Material response and perturbation equations

Let $\xi(r)e^{i\omega t}$ denote the radial displacement and let Δ_L and δ denote Lagrangian and Eulerian perturbations, respectively, so that $\Delta_L F = \delta F + \xi\, dF/dr$. The equilibrium parameters η and ρ_s are held fixed during each oscillation. Consequently,

$$\Delta_L P_r = \eta\, \Delta_L \rho. \tag{97}$$

Writing $\Sigma = P_t - P_r$ for the physical anisotropy, we introduce a material label a_L that is transported with each fluid layer and prescribe

$$\Sigma(a_L, \rho) = \Sigma_0(a_L) \left[\frac{\rho + P_r}{\rho_0(a_L) + P_{r0}(a_L)}\right]^{\kappa}, \qquad \kappa = 0, 1. \tag{98}$$

The subscript 0 denotes the chosen background. For $\kappa = 0$, each layer preserves its anisotropy, whereas for $\kappa = 1$ it preserves $\Sigma/(\rho + P_r)$. These are phenomenological response laws; they are not deduced from the equilibrium equation of state or from gravitational decoupling. Both preserve the central behavior $\Sigma = O(r^2)$ on the regular perturbative branch. Their linearization gives

$$\Delta_L \Sigma = \frac{\kappa(1+\eta)\Sigma}{\eta(\rho + P_r)} \Delta_L P_r. \tag{99}$$

In particular, $\Delta_L \Sigma = 0$ and $\delta\Sigma = 0$ are different prescriptions.

The dynamic response of anisotropic stresses cannot be uniquely determined from the radial equilibrium equation of state. To address this, an additional constitutive prescription is required to close the system of radial perturbations. In this regard, previous studies have demonstrated the importance of anisotropic equations of state and stress prescriptions for determining the radial stability and oscillation spectra of compact stars [22, 48, 49, 87]. In this work, the choice $\kappa = 0$ represents an anisotropy that is "frozen" in the Lagrangian sense, while $\kappa = 1$ defines the ratio between the anisotropy and the enthalpy as fluid elements undergo displacement. These two prescriptions are adopted as phenomenological limiting cases rather than as derived microscopic laws. Consequently, the resulting frequencies and conclusions regarding stability must be understood as being contingent upon the assumed anisotropic constitutive behaviour. Furthermore, it should be noted that future work could examine the full range $0 \le \kappa \le 1$ to determine how the spectrum $\omega_n^2(\kappa)$ evolves continuously.

For the numerical problem we use $x = r/R$, $H = e^{-\lambda}$, $b = e^{\nu} = 1 - 3u + ux^2$, and the dimensionless background variables

$$\begin{aligned} &\varepsilon = 8\pi R^2 \rho, && p = 8\pi R^2 P_r, \\ &\sigma = 8\pi R^2 (P_t - P_r), && w = \varepsilon + p. \end{aligned} \tag{100}$$

The factors in Eq. (100) use geometrized units, $G = c = 1$. We define

$$y = \frac{\xi}{r}, \qquad d = 8\pi R^2 \Delta_L P_r, \qquad q = \left(\frac{\omega R}{c_{\rm light}}\right)^2. \tag{101}$$

Primes in this section denote differentiation with respect to x. Linearizing the Einstein constraints and radial stress-energy conservation, including the metric perturbations, gives

$$y' = a_y y + B_d d, \tag{102}$$

$$d' = (C_y + qW_y) y + E_d d, \tag{103}$$

where

$$
\begin{aligned}
a_y &= \frac{\nu'}{2} - \frac{3}{x} - \frac{2\sigma}{wx},\\
B_d &= -\frac{1}{\eta w x},\\
C_y &= -4p' - \frac{wpx}{H} + \frac{xw\nu'^2}{4} + \frac{2\sigma}{x}\\
&\quad + 2\sigma\nu' - \frac{4\sigma^2}{wx},\\
W_y &= \frac{wx}{Hb},
\end{aligned}
\tag{104}
$$

$$
E_d = -\frac{\nu'}{2} - \frac{wx}{2H} + \frac{2[\kappa(1+\eta)-1]\sigma}{\eta w x}. \tag{105}
$$

$$
\begin{aligned}
\delta\lambda &= -\frac{x^2 w y}{H},\\
\delta\nu' &= \left(\nu' + \frac{1}{x}\right)\delta\lambda + \frac{x\,\delta p}{H},
\end{aligned}
\tag{106}
$$

For example, the metric constraints used in this reduction are

with $\delta p = d - xyp'$ and $\delta\varepsilon = d/\eta - xy\varepsilon'$. The anisotropy perturbation is

$$
\delta\sigma = \frac{\kappa(1+\eta)\sigma}{\eta w} d - xy\sigma'. \tag{107}
$$

Thus the calculation does not freeze the metric or infer a dynamical anisotropy law from the ratio P_t'/ρ' of the equilibrium profiles.

6.2 Boundary conditions and spectral problem

Regularity at the center fixes the relation between the two perturbation variables. Choosing the arbitrary linear normalization $y(0) = 1$ gives

$$
d(0) = -3\eta w(0), \qquad \xi(0) = 0. \tag{108}
$$

The regular even-power expansion through x^6 supplies initial data close to the center; it is used only to start the integration. The surface moves with the fluid, and the appropriate free-boundary condition is

$$
\Delta_L P_r(R) = 0, \qquad \text{or equivalently} \qquad d(1) = 0. \tag{109}
$$

Neither $\delta P_r(R) = 0$ at fixed radius nor $P_t(R) = 0$ is imposed. For the response law above, Eq. (110) also implies $\Delta_L\rho(R) = \Delta_L\Sigma(R) = 0$. The nonzero equilibrium surface density therefore causes no singular coefficient: although $\Gamma_r = \eta(\rho + P_r)/P_r$ diverges as $P_r \to 0$, the combination $\Gamma_r P_r = \eta(\rho + P_r)$ entering the equations remains finite.

Eliminating d yields

$$
y'' = A_2 y' + (V_0 - qV_1)y, \tag{110}
$$

where

$$
\begin{aligned}
A_2 &= a_y + E_d + B_d'/B_d,\\
V_0 &= a_y' + B_d C_y - a_y(E_d + B_d'/B_d),\\
V_1 &= -B_d W_y = \frac{1}{\eta H b} > 0.
\end{aligned}
\tag{111}
$$

With $\mathcal{P} = \exp[-\int A_2\,dx] > 0$, $\mathcal{Q} = \mathcal{P}V_0$ and $\mathcal{W} = \mathcal{P}V_1$, this becomes

$$
-(\mathcal{P}y')' + \mathcal{Q}y = q\mathcal{W}y. \tag{112}
$$

Here $\mathcal{P} \sim x^4$ at the center; the irregular solution $y \sim x^{-3}$ is excluded. At the surface, $y'(1) = a_y(1)y(1)$. Accordingly, the Rayleigh quotient includes the surface term,

$$
q = \frac{\displaystyle\int_0^1 (\mathcal{P}y'^2 + \mathcal{Q}y^2)\,dx - \mathcal{P}(1)a_y(1)y(1)^2}{\displaystyle\int_0^1 \mathcal{W}y^2\,dx}. \tag{113}
$$

For this real conservative problem, the fundamental mode is nodeless. The condition $q_0 > 0$ implies linear radial stability under the specified closure, whereas $q_0 < 0$ corresponds to exponential growth.

6.3 Numerical spectra and mode profiles

We computed the fundamental mode and the first three radial overtones for each of the twelve backgrounds and both values of κ, obtaining 96 eigenvalues. A continuous Prüfer-phase search includes the negative q region and is followed by shooting refinement of Eqs. (102) and (103). For every background and closure, positivity checks with exact rational Bernstein coefficients establish $V_0/V_1 + 100 \geq 0$ on $0 \leq x \leq 1$, and $a_y(1) \leq 0$. Equation (114) then gives the lower bound $q \geq -100$, which sets the lower end of the spectral search.

The displacement eigenfunctions have respectively zero, one, two and three interior nodes. Changing arithmetic precision and the central starting point changes the eigenvalues by less than 2.4×10^{-17} in the recorded comparisons. The maximum normalized surface residual is 6.0×10^{-23}; agreement with the Rayleigh quotient and the maximum normalized overlap of distinct modes are better than 2.8×10^{-18} and 5.1×10^{-18}, respectively. An independent implementation of the linearized Einstein and conservation equations agrees within 5.7×10^{-14}. The latter refines the previously located roots and is not an independent global spectral search. These figures quantify numerical consistency, not physical uncertainty or rigorous interval bounds on the eigenvalues.

Table 2 Fundamental eigenvalue $q_0 = (\omega_0 R/c)^2$ for the twelve equilibrium configurations and the two material responses in Eq. (98).

η	u	q_0 ($\kappa = 0$)	q_0 ($\kappa = 1$)
1	0.100	5.89513198	5.72364703
1	0.148	4.28679684	4.05634429
1	0.196	2.87569435	2.60583884
1/2	0.227	0.82625953	0.70995096
1/2	0.243	0.62339139	0.51179733
1/2	0.259	0.43076829	0.32740594
1/3	0.181	0.85825179	0.81078068
1/3	0.213	0.53611931	0.49416880
1/3	0.244	0.25342893	0.22409548
1/4	0.158	0.74799673	0.73940730
1/4	0.200	0.39547955	0.39700572
1/4	0.241	0.09244687	0.11232334

Table 2 and the fundamental-mode figures below give the fundamental eigenvalues. All 24 background–closure combinations have $q_0 > 0$. Within each sampled family and each closure, q_0 decreases as u increases. The smallest value is $q_0 = 0.09244687$ for $\eta = 1/4$, $u = 0.241$ and $\kappa = 0$; its sign remains positive. The effect of changing the material response is not universal: $\kappa = 1$ lowers q_0 in the sampled $\eta = 1, 1/2, 1/3$ families, whereas for $\eta = 1/4$ it lowers q_0 at $u = 0.158$ and raises it at $u = 0.200$ and 0.241. No stability boundary is extrapolated from these three-point samples. For example, at $\eta = 1/4$ and $u = 0.241$, changing from $\kappa = 0$ to $\kappa = 1$ increases q_0 from 0.09244687 to 0.11232334, a relative increase of approximately 21.5%. Because the background and its radius are unchanged, the corresponding fundamental frequency increases by approximately 10.2%, as follows from $f \propto \sqrt{q_0}$. This quantifies the sensitivity of the radial spectrum to the adopted anisotropic response even when the equilibrium configuration is fixed.

The computed positivity of q_0 establishes stability against the radial perturbations defined above, but it does not establish stability for an arbitrary anisotropic material law. In particular, it does not remove the equilibrium limitations associated with the $\eta = 1$ family or justify regions of tangential tension as a microscopic model of quark matter. Nonradial stability, full characteristic causality and observational viability require additional analysis. Moreover, the response laws are constructed around each background; the sampled models are not by themselves a continuous sequence with a single globally specified material law. We therefore do not replace the eigenvalue calculation by a mass-turning-point argument.

Finally, the exterior matching fixes the time normalization. Once a physical radius is specified, the corresponding cyclic frequency is

$$f = \frac{c}{2\pi R}\sqrt{q}. \tag{115}$$

The radius also fixes the density scale through $8\pi R^2 \rho_s$ in geometrized units. We therefore report dimensionless eigenvalues and do not assign a frequency in kilohertz without specifying that scale.

To illustrate the physical scale of the results, we have constructed Table 3, for which we have assumed $\rho_s = 240\,\mathrm{MeV/fm^3}$—a value that corresponds to $B = 60\,\mathrm{MeV/fm^3}$ when $\eta = 1/3$ and $\rho_s = 4B$. For other stiffness values, the same surface density is adopted as a reference, without implying that their equations of state follow the MIT model. In SI units, letting ϵ_s represent this energy density, we use $R = [sc^4/(8\pi G\epsilon_s)]^{1/2}$, $M = uRc^2/G$, and Eq. (115), with s defined by Eq. (85). The values are calculated based on the eigenvalues provided in Table 2. As the scale varies, M and R are proportional to $\rho_s^{-1/2}$, while f_0 is proportional to $\rho_s^{1/2}$.

As an astrophysical reference, Gangopadhyay et al. [88] studied strange stars with masses on the order of 1–2 $M_\odot$ and compact radii; their model reaches a maximum mass of $2.0545\,M_\odot$ with a radius of 9.5 km. The scales in Table 3 allow us to place our configurations within the dimensional context of these models. This comparison is intended for guidance only: the equations of state and the assumptions regarding stresses differ, and it does not constitute a fit to those pulsars, nor does it determine the maximum mass for our families of stars. Furthermore, it does not provide an observational validation of the calculated frequencies.

The frequency scales in Table 3 can also be placed in the context of previous radial-oscillation studies. Vásquez Flores and Lugones [21] found fundamental periods of approximately 0.1 ms for low-mass self-bound quark stars within a color-superconducting MIT bag framework, corresponding to frequencies of order 10 kHz. Pretel et al. [85] further investigated how anisotropic pressure affects the masses, radii and radial oscillation spectra of interacting quark stars. These studies provide complementary context for our dimensional results; differences in the equations of state and anisotropic response prescriptions preclude a direct quantitative identification of their spectra with ours.

The following individual figures display all 96 modes, with displacement and Lagrangian pressure perturbation shown separately. Each curve is divided by its own maximum absolute value over the stored radial grid, so that the figures compare radial shapes rather than amplitudes:

$$\widehat{\xi} = \frac{\xi}{\max|\xi|}, \qquad \widehat{\Delta_L P_r} = \frac{\Delta_L P_r}{\max|\Delta_L P_r|}. \tag{116}$$

Table 3 Dimensional scales of the twelve configurations for an illustrative surface density $\rho_s = 240\,\mathrm{MeV/fm^3}$. The frequencies correspond to the fundamental mode and the two constitutive responses of the manuscript.

η	u	$M/M_\odot$	R (km)	$f_0^{(\kappa=0)}$ (kHz)	$f_0^{(\kappa=1)}$ (kHz)
1	0.100	0.574	8.478	13.665	13.465
1	0.148	1.016	10.140	9.742	9.477
1	0.196	1.511	11.382	7.109	6.767
1/2	0.227	1.742	11.334	3.827	3.547
1/2	0.243	1.885	11.454	3.289	2.980
1/2	0.259	2.017	11.501	2.723	2.374
1/3	0.181	1.273	10.384	4.257	4.138
1/3	0.213	1.562	10.828	3.226	3.098
1/3	0.244	1.822	11.029	2.178	2.048
1/4	0.158	1.047	9.782	4.219	4.194
1/4	0.200	1.417	10.464	2.867	2.873
1/4	0.241	1.755	10.751	1.349	1.487

The common integration normalization is $y(0) = 1$; the amplitude of a linear eigenmode remains arbitrary. The absolute displacement vanishes at the center, while the Lagrangian pressure perturbation vanishes at the surface. The additional displacement nodes distinguish the three overtones from the fundamental mode. Each mode profile is drawn as a solid colored line.

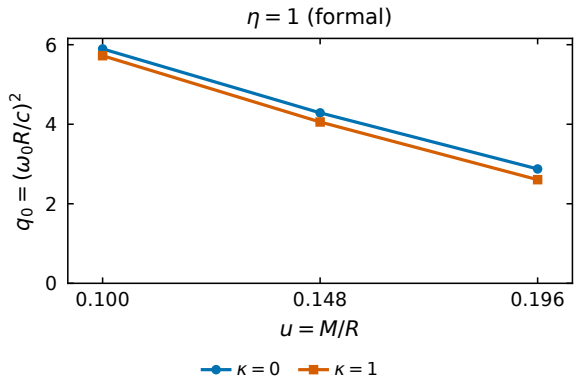


Fig. 7 Fundamental radial eigenvalue q_0 for $\eta = 1$ and $\kappa = 0, 1$. Solid lines join the three computed points as visual guides, without defining a continuously calculated sequence.

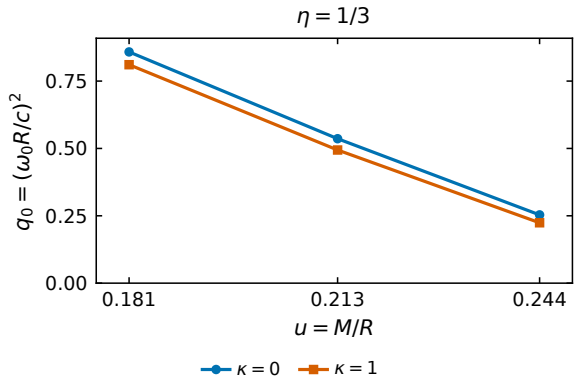


Fig. 8 Fundamental radial eigenvalue q_0 for $\eta = 1/3$ and $\kappa = 0, 1$. Solid lines join the three computed points as visual guides, without defining a continuously calculated sequence.

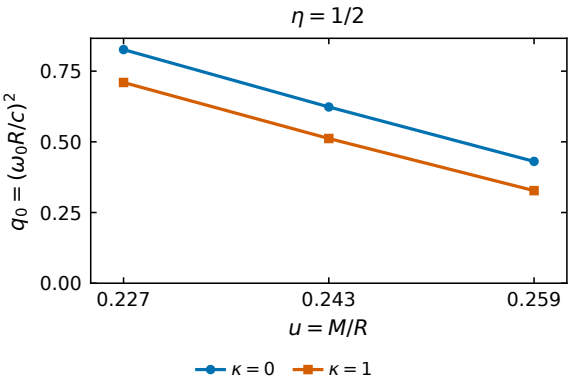


Fig. 9 Fundamental radial eigenvalue q_0 for $\eta = 1/2$ and $\kappa = 0, 1$. Solid lines join the three computed points as visual guides, without defining a continuously calculated sequence.

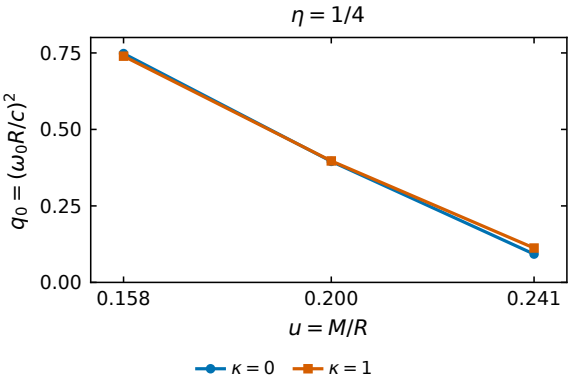


Fig. 10 Fundamental radial eigenvalue q_0 for $\eta = 1/4$ and $\kappa = 0, 1$. Solid lines join the three computed points as visual guides, without defining a continuously calculated sequence.

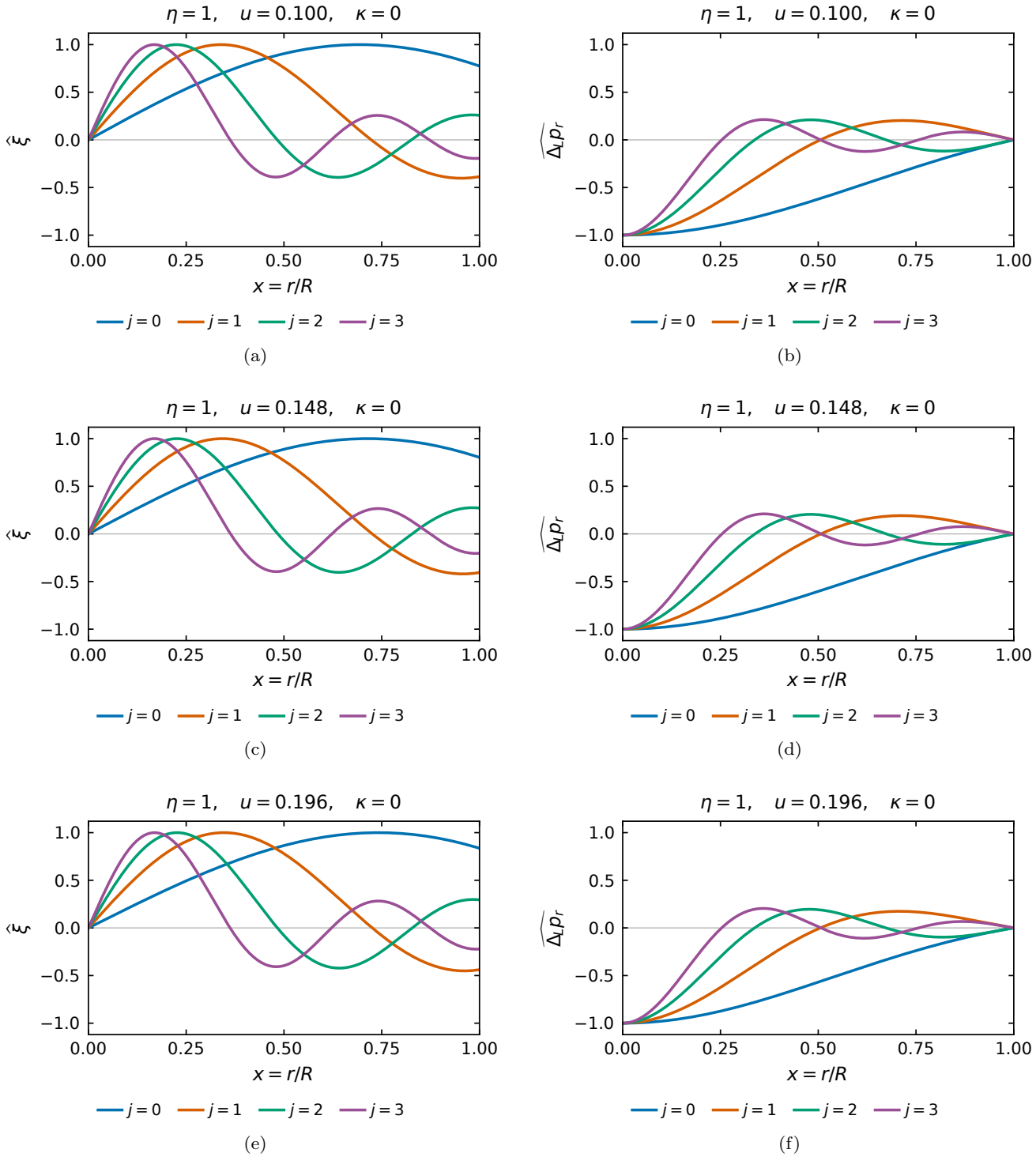


Fig. 11 Normalized radial modes for $\eta = 1$ and $\kappa = 0$. (a) $\widehat{\xi}$ and (b) $\widehat{\Delta_L P_r}$ for $u = 0.100$; (c) $\widehat{\xi}$ and (d) $\widehat{\Delta_L P_r}$ for $u = 0.148$; (e) $\widehat{\xi}$ and (f) $\widehat{\Delta_L P_r}$ for $u = 0.196$. Each panel shows modes $j = 0, 1, 2, 3$ as solid colored curves, normalized separately as in Eq. (116).

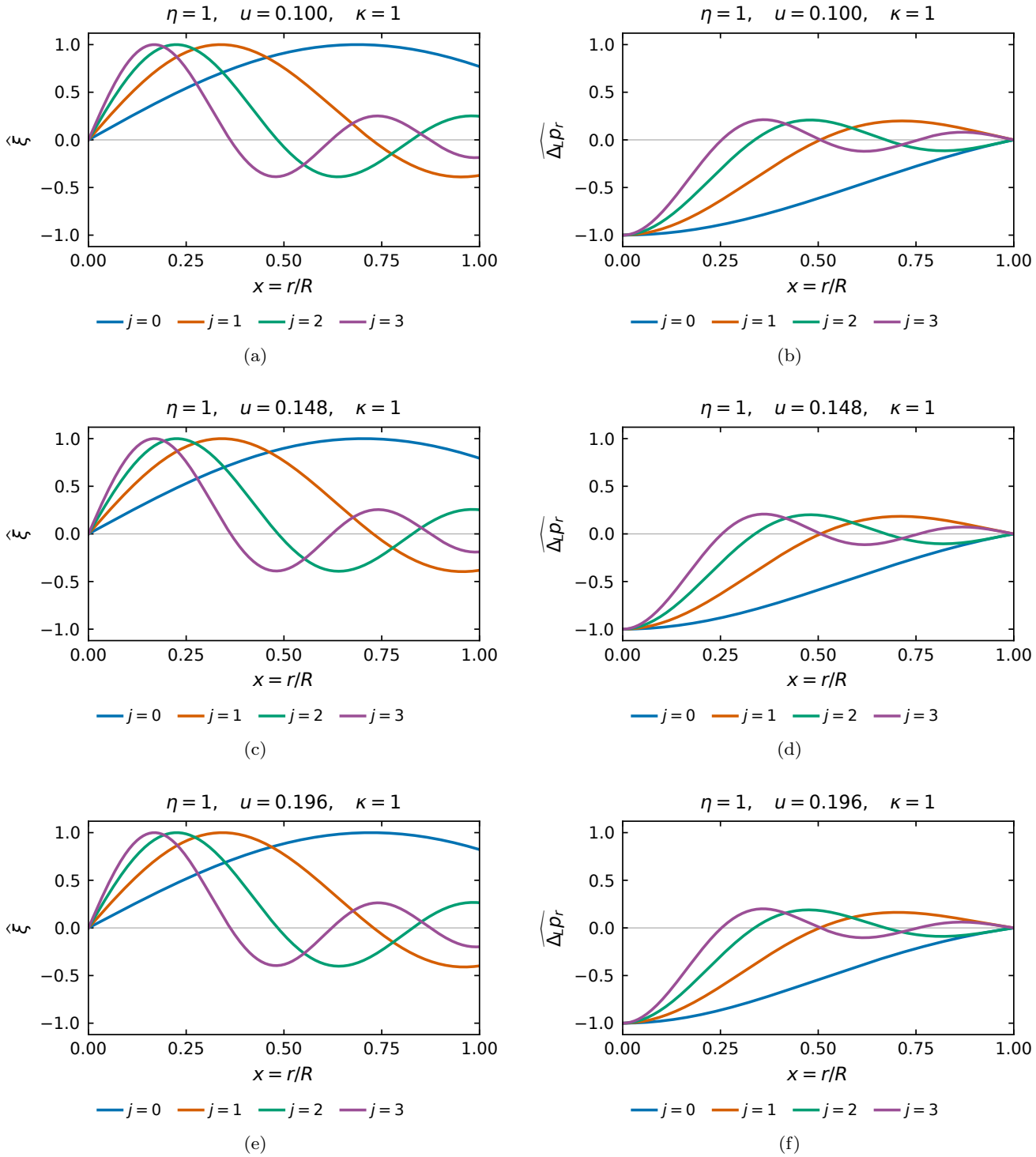


Fig. 12 Normalized radial modes for $\eta = 1$ and $\kappa = 1$. (a) $\widehat{\xi}$ and (b) $\widehat{\Delta_L P_r}$ for $u = 0.100$; (c) $\widehat{\xi}$ and (d) $\widehat{\Delta_L P_r}$ for $u = 0.148$; (e) $\widehat{\xi}$ and (f) $\widehat{\Delta_L P_r}$ for $u = 0.196$. Each panel shows modes $j = 0, 1, 2, 3$ as solid colored curves, normalized separately as in Eq. (116).

For $\eta = 1$, the individual profiles in Figs. 11a–12f retain the stiff family as a formal comparison. Both material responses give positive fundamental eigenvalues at the three compactnesses shown. The spectral result does not remove the physical reservations about this equilibrium family discussed above.

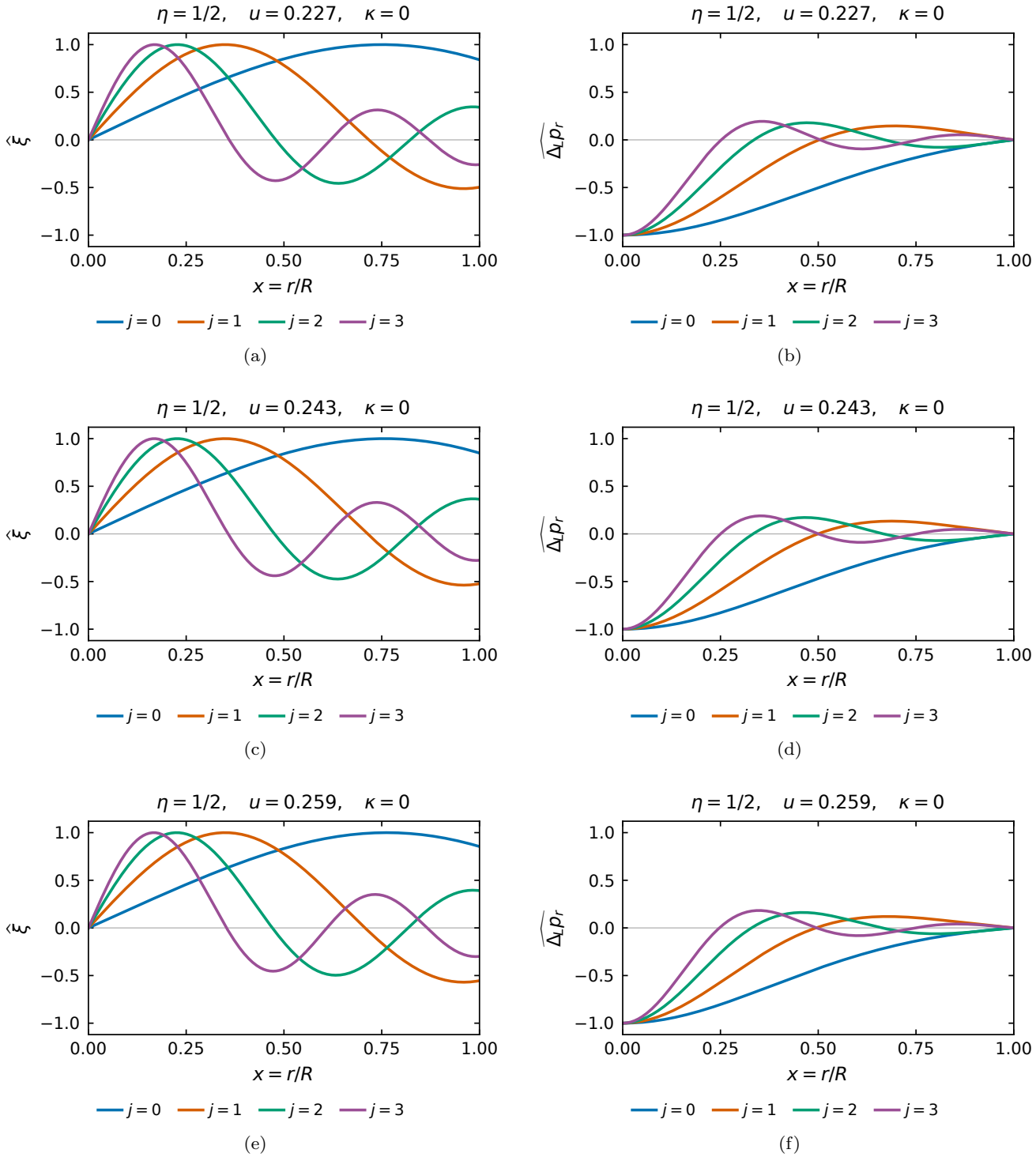


Fig. 13 Normalized radial modes for $\eta = 1/2$ and $\kappa = 0$. (a) $\widehat{\xi}$ and (b) $\widehat{\Delta_L P_r}$ for $u = 0.227$; (c) $\widehat{\xi}$ and (d) $\widehat{\Delta_L P_r}$ for $u = 0.243$; (e) $\widehat{\xi}$ and (f) $\widehat{\Delta_L P_r}$ for $u = 0.259$. Each panel shows modes $j = 0, 1, 2, 3$ as solid colored curves, normalized separately as in Eq. (116).

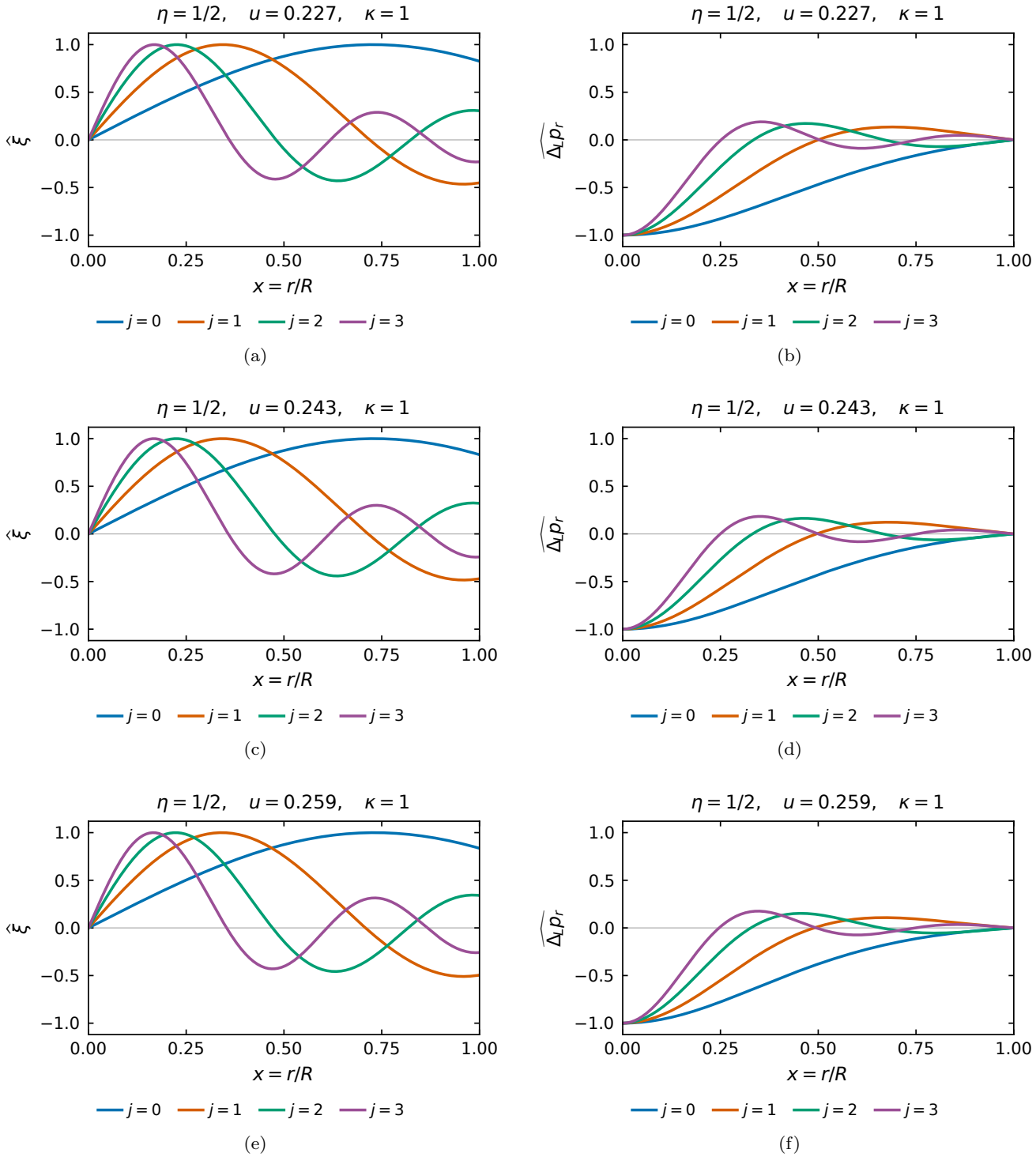


Fig. 14 Normalized radial modes for $\eta = 1/2$ and $\kappa = 1$. (a) $\widehat{\xi}$ and (b) $\widehat{\Delta_L P_r}$ for $u = 0.227$; (c) $\widehat{\xi}$ and (d) $\widehat{\Delta_L P_r}$ for $u = 0.243$; (e) $\widehat{\xi}$ and (f) $\widehat{\Delta_L P_r}$ for $u = 0.259$. Each panel shows modes $j = 0, 1, 2, 3$ as solid colored curves, normalized separately as in Eq. (116).

For $\eta = 1/2$, Figs. 13a–14f show the displacement and pressure response at $u = 0.227, 0.243, 0.259$. The fundamental eigenvalue remains positive and decreases across these sampled compactnesses for both closures. Changing the closure also changes the eigenfunctions, even though the equilibrium is held fixed.

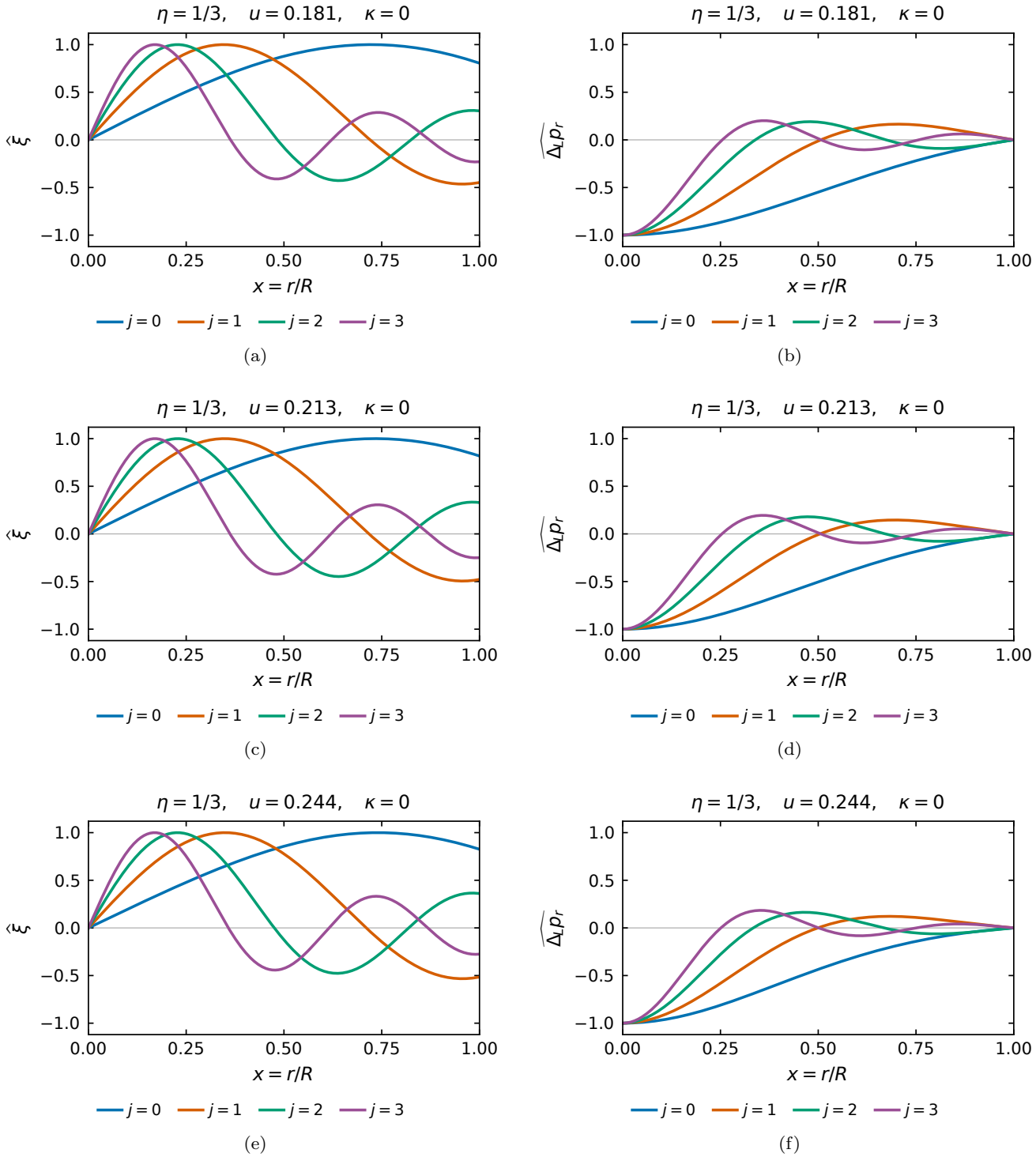


Fig. 15 Normalized radial modes for $\eta = 1/3$ and $\kappa = 0$. (a) $\widehat{\xi}$ and (b) $\widehat{\Delta_L P_r}$ for $u = 0.181$; (c) $\widehat{\xi}$ and (d) $\widehat{\Delta_L P_r}$ for $u = 0.213$; (e) $\widehat{\xi}$ and (f) $\widehat{\Delta_L P_r}$ for $u = 0.244$. Each panel shows modes $j = 0, 1, 2, 3$ as solid colored curves, normalized separately as in Eq. (116).

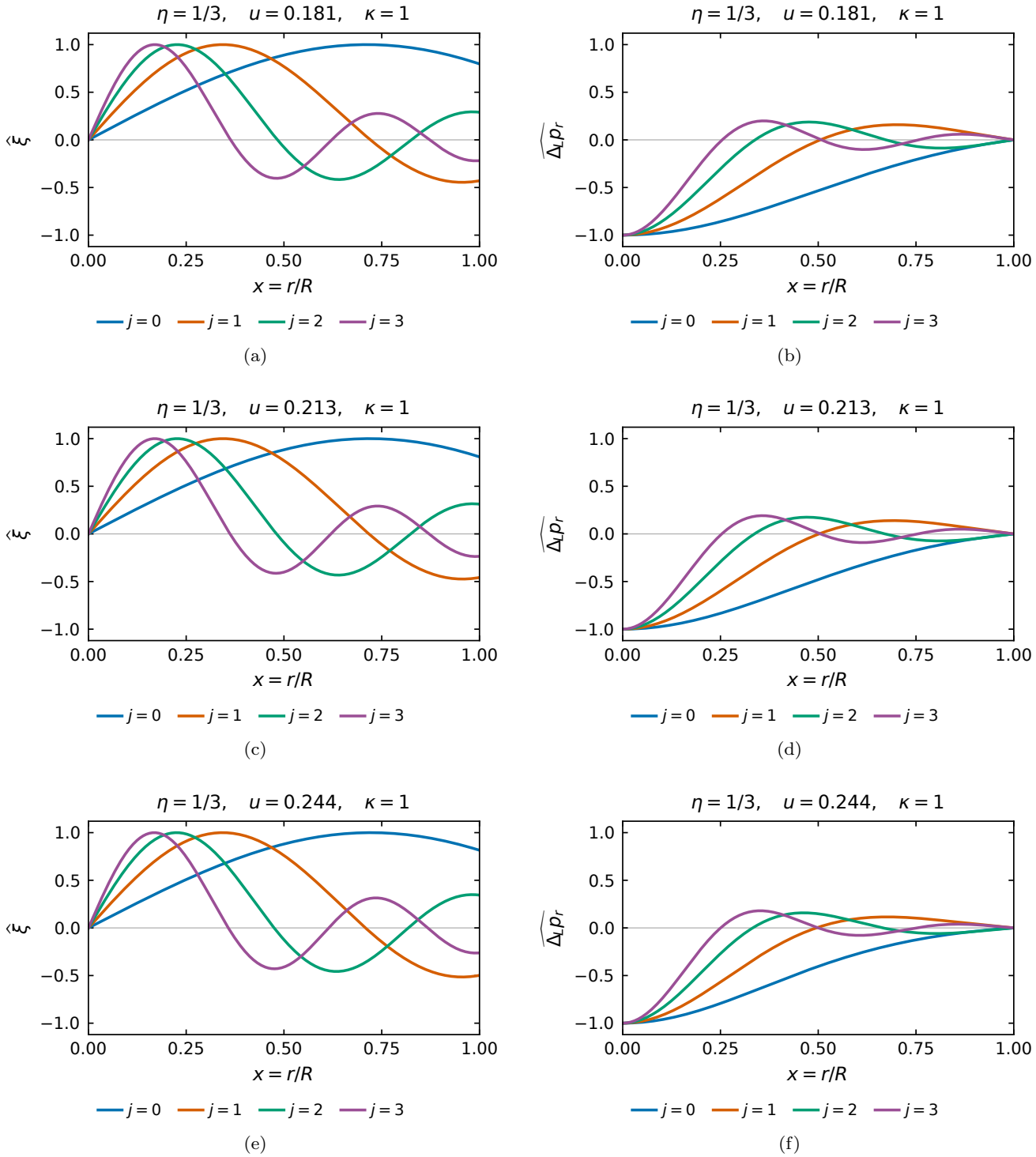


Fig. 16 Normalized radial modes for $\eta = 1/3$ and $\kappa = 1$. (a) $\widehat{\xi}$ and (b) $\widehat{\Delta_L P_r}$ for $u = 0.181$; (c) $\widehat{\xi}$ and (d) $\widehat{\Delta_L P_r}$ for $u = 0.213$; (e) $\widehat{\xi}$ and (f) $\widehat{\Delta_L P_r}$ for $u = 0.244$. Each panel shows modes $j = 0, 1, 2, 3$ as solid colored curves, normalized separately as in Eq. (116).

For $\eta = 1/3$, Figs. 15a–16f show all four modes at $u = 0.181, 0.213, 0.244$. The displacement profiles exhibit the expected progression from the nodeless fundamental mode to three nodes in the third overtone. The surface condition applies to the Lagrangian pressure perturbation in each of the accompanying profiles.

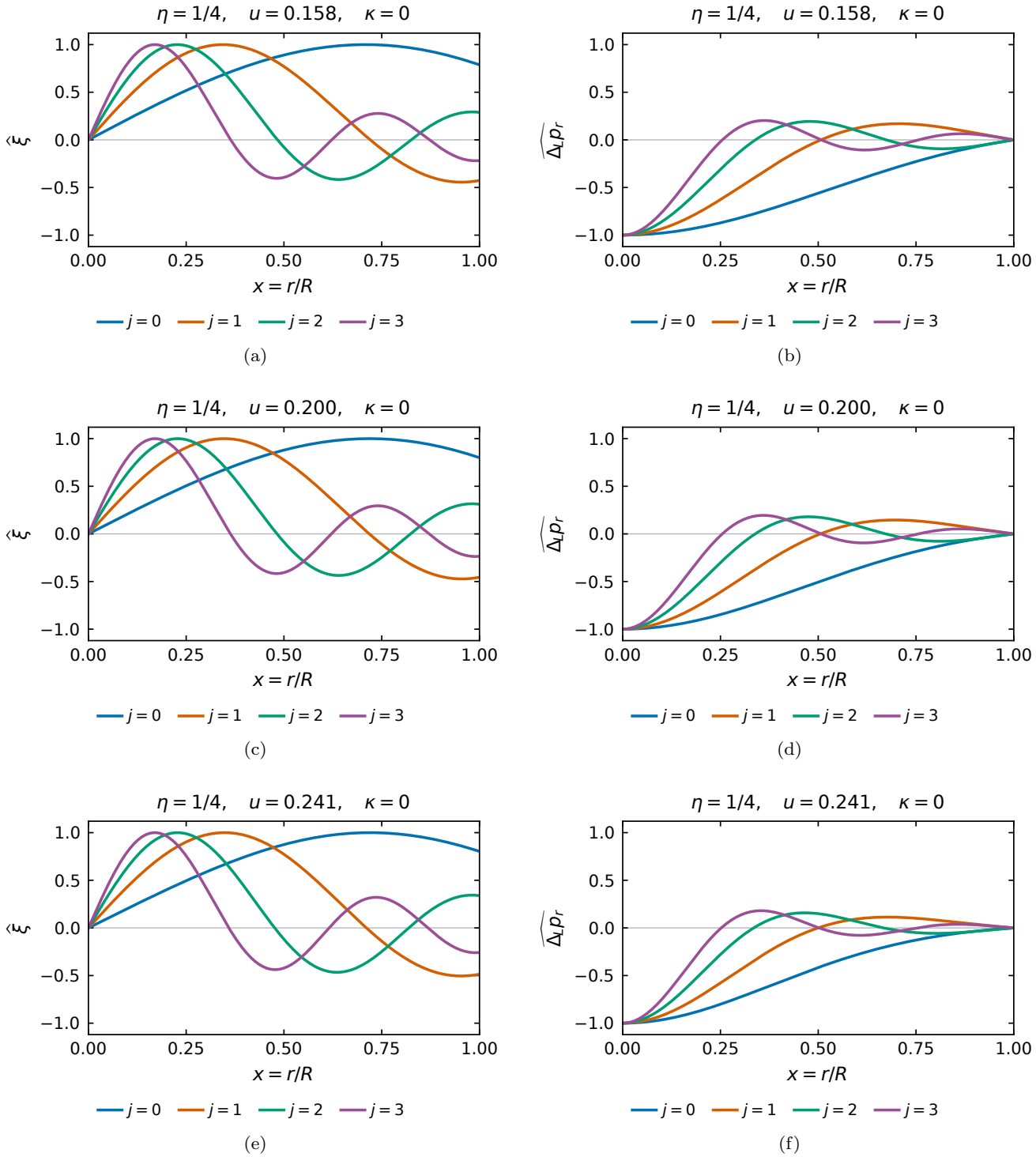


Fig. 17 Normalized radial modes for $\eta = 1/4$ and $\kappa = 0$. (a) $\widehat{\xi}$ and (b) $\widehat{\Delta_L P_r}$ for $u = 0.158$; (c) $\widehat{\xi}$ and (d) $\widehat{\Delta_L P_r}$ for $u = 0.200$; (e) $\widehat{\xi}$ and (f) $\widehat{\Delta_L P_r}$ for $u = 0.241$. Each panel shows modes $j = 0, 1, 2, 3$ as solid colored curves, normalized separately as in Eq. (116).

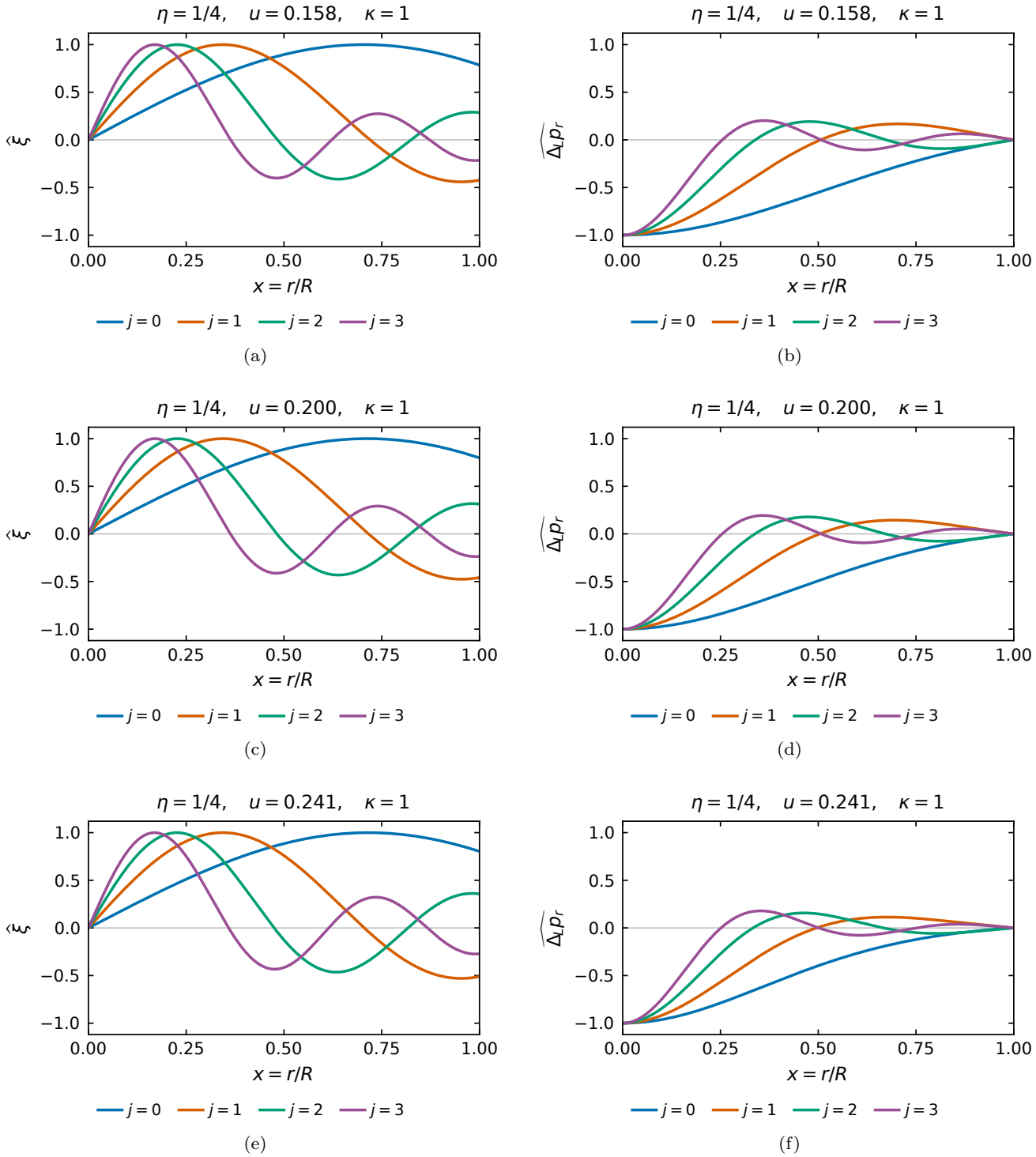


Fig. 18 Normalized radial modes for $\eta = 1/4$ and $\kappa = 1$. (a) $\widehat{\xi}$ and (b) $\widehat{\Delta_L P_r}$ for $u = 0.158$; (c) $\widehat{\xi}$ and (d) $\widehat{\Delta_L P_r}$ for $u = 0.200$; (e) $\widehat{\xi}$ and (f) $\widehat{\Delta_L P_r}$ for $u = 0.241$. Each panel shows modes $j = 0, 1, 2, 3$ as solid colored curves, normalized separately as in Eq. (116).

For $\eta = 1/4$, Figs. 17a–18f complete the mode comparison at $u = 0.158, 0.200, 0.241$. This family contains the smallest computed fundamental eigenvalue. Both closures still give $q_0 > 0$, while their ordering changes between the lowest and the two higher sampled compactnesses.

7 Discussion and conclusions

The present construction supplements EFEs with two explicit assumptions: the Tolman IV temporal potential and a generalized linear EoS for the complete energy density and radial pressure. The EoS determines the radial deformation, and the remaining field equation determines the tangential stress. This separates the geometric choice defining the equilibrium family from the material-response prescriptions needed to determine its radial spectrum.

The field equations involve the metric potentials and the thermodynamic variables ρ, P_r and $P_\perp$, and therefore require additional relations to form a closed system. In our construction, the prescribed temporal potential and the radial relation $P_r = \eta(\rho - \rho_s)$ determine the complete radial metric potential, after central regularity and Schwarzschild matching are imposed. The tangential pressure and the anisotropy then follow from the remaining field equation. Thus, the radial EoS does not independently prescribe the tangential sector, and minimal geometric deformation provides a consistent representation of the additional source rather than a microscopic explanation of its stresses. The resulting equilibrium solution admits a closed rational representation in terms of finite polynomial sums for $\eta = 1, 1/2, 1/3$ and $1/4$.

The generalized linear parametrization separates the stiffness of the radial response, controlled by η, from the surface-density scale set by ρ_s. This separation provides a framework for investigating changes in stellar structure and oscillation spectra, but the parameters of the matched family cannot all be varied independently. In particular, Eq. (85) fixes $s = 8\pi R^2 \rho_s$ once u and η are chosen. At fixed u and η, the dimensional mass and radius therefore scale as $\rho_s^{-1/2}$, while the oscillation frequencies scale as $\rho_s^{1/2}$. Comparisons at fixed physical EoS must respect this scaling; plots with $R = 1$ do not represent stars with a common dimensional radius.

For $\eta = 1/3$ and $\rho_s = 4B$, the radial EoS reduces to the simplest MIT bag relation. This identifies a thermodynamic limit of the radial sector, without making the complete anisotropic configuration equivalent to an isotropic MIT bag star. The finite interior surface density follows from $P_r(R) = 0$ and represents the self-bound boundary of the model. The displayed equilibria are regular and satisfy the reported energy inequalities, but their tangential stresses distinguish the families. Tangential tension occurs near the surface in the sampled $\eta = 1$ and $\eta = 1/2$ configurations and in the two less compact $\eta = 1/3$ examples. By contrast, $P_\perp$ remains positive in the sampled $\eta = 1/4$ models and in the $\eta = 1/3$, $u = 0.244$ configuration. The $\eta = 1$ family also fails the adopted subluminal tangential-profile diagnostic and is retained only as a formal comparison. Neither the energy inequalities nor radial-mode stability removes these limitations.

The distinction between equilibrium closure and dynamical closure is essential. A static anisotropy profile does not determine its response to a fluid displacement, so two material prescriptions were specified: conservation of the anisotropy carried by each layer for $\kappa = 0$, and conservation of its ratio to $\rho + P_r$ for $\kappa = 1$. Both reproduce the same background while defining different perturbation problems. With metric perturbations included, central regularity and the moving-surface condition $\Delta_L P_r(R) = 0$ yield the radial spectrum. The nonzero surface density causes no singularity in the relevant adiabatic coefficient, since $\Gamma_r P_r = \eta(\rho + P_r)$ remains finite even though Γ_r diverges as the radial pressure vanishes.

The fundamental mode and the first three overtones were computed for twelve backgrounds and both material prescriptions, giving 96 eigenvalues. All 24 background–closure combinations have a positive fundamental eigenvalue and are therefore linearly stable against the specified radial perturbations. Within each sampled stiffness family, q_0 decreases with increasing compactness for both closures. The smallest reported value is $q_0 = 0.09244687$, obtained for $\eta = 1/4$, $u = 0.241$ and $\kappa = 0$. Nevertheless, changing the anisotropic response does not produce a universal shift: $\kappa = 1$ lowers the fundamental eigenvalue in the sampled $\eta = 1, 1/2, 1/3$ families, whereas the ordering reverses at the two larger compactnesses of the $\eta = 1/4$ family. At $\eta = 1/4$ and $u = 0.241$, this change of response increases the fundamental frequency by approximately 10.2% at fixed background, despite leaving the equilibrium geometry unchanged. The equilibrium geometry alone is therefore insufficient to determine the radial spectrum.

The importance of specifying the anisotropic response and the surface conditions is consistent with the analysis of Arbañil and Malheiro [22], who showed that the relation between maximum mass and the onset of radial instability in anisotropic strange stars depends on the equilibrium sequence and its surface anisotropy. Our discrete samples, with response laws defined around each background, do not establish a continuous sequence governed by a single global material prescription. Consequently, the present results neither identify a maximum stable mass nor locate a critical compactness where the fundamental mode vanishes. They also do not establish nonradial stability, full characteristic causality or agreement with observational constraints.

Finally, the main outcome is an analytically tractable family of self-bound anisotropic equilibria together with a radial stability analysis that explicitly separates the assumptions defining the background from those defining its material response. Extending the calculation to continuous sequences at fixed surface density and with a globally specified anisotropic constitutive law would allow stability boundaries and mass-radius relations to be assessed consistently. A microscopic account of the tangential stresses, particularly in regions of tension, and an analysis of nonradial modes and tidal response are further steps needed to evaluate the astrophysical interpretation of these configurations.

References

1. M. Camenzind, *Compact Objects in Astrophysics*, Springer (2007).
2. S. Huth et al., *Constraining neutron-star matter with microscopic and macroscopic collisions*, Nature **606**, 276–280 (2022).
3. N. K. Glendenning, *Compact Stars: Nuclear Physics, Particle Physics, and General Relativity*, 2nd ed., Springer, New York (2000).
4. P. Haensel, A. Y. Potekhin and D. G. Yakovlev, *Neutron Stars 1: Equation of State and Structure*, Astrophysics and Space Science Library, Vol. 326, Springer, New York (2007).
5. S. L. Shapiro and S. A. Teukolsky, *Black Holes, White Dwarfs, and Neutron Stars: The Physics of Compact Objects*, Wiley, New York (1983).
6. J. M. Lattimer and M. Prakash, *The Equation of State of Hot, Dense Matter and Neutron Stars*, Phys. Rep. **621**, 127–164 (2016).
7. F. Weber, *Strange Quark Matter and Compact Stars*, Prog. Part. Nucl. Phys. **54**, 193–288 (2005).
8. P. B. Demorest, T. Pennucci, S. M. Ransom, M. S. E. Roberts and J. W. T. Hessels, *A Two-Solar-Mass Neutron Star Measured Using Shapiro Delay*, Nature **467**, 1081–1083 (2010).
9. E. Fonseca et al., *The NANOGrav Nine-year Data Set: Mass and Geometric Measurements of Binary Millisecond Pulsars*, Astrophys. J. **832**, 167 (2016).
10. J. Antoniadis et al., *A Massive Pulsar in a Compact Relativistic Binary*, Science **340**, 1233232 (2013).
11. H. T. Cromartie et al., *Relativistic Shapiro Delay Measurements of an Extremely Massive Millisecond Pulsar*, Nat. Astron. **4**, 72–76 (2020).
12. K. C. Gendreau et al., *The Neutron Star Interior Composition Explorer (NICER): Design and Development*, Proc. SPIE **9905**, 99051H (2016).
13. M. C. Miller et al., *The Radius of PSR J0740+6620 from NICER and XMM-Newton Data*, Astrophys. J. Lett. **918**, L28 (2021).
14. T. E. Riley et al., *A NICER View of the Massive Pulsar PSR J0740+6620 Informed by Radio Timing and XMM-Newton Spectroscopy*, Astrophys. J. Lett. **918**, L27 (2021).
15. K. Nandra et al., *The Hot and Energetic Universe: A White Paper Presenting the Science Theme Motivating the Athena+ Mission*, arXiv:1306.2307 [astro-ph.HE] (2013).
16. M. Feroci et al., *The Large Observatory for X-ray Timing (LOFT)*, Exp. Astron. **34**, 415–444 (2012).
17. B. P. Abbott et al., *Multi-messenger Observations of a Binary Neutron Star Merger*, Astrophys. J. Lett. **848**, L12 (2017).
18. B. P. Abbott et al., *GW170817: Measurements of Neutron Star Radii and Equation of State*, Phys. Rev. Lett. **121**, 161101 (2018).
19. M. Alford, M. Braby, M. Paris and S. Reddy, *Hybrid Stars That Masquerade as Neutron Stars*, Astrophys. J. **629**, 969–978 (2005).
20. O. Lourenço, C. H. Lenzi, M. Dutra, E. J. Ferrer, V. de la Incera, L. Paulucci and J. E. Horvath, *Tidal Deformability of Strange Stars and the GW170817 Event*, Phys. Rev. D **103**, 103010 (2021).
21. C. Vásquez Flores and G. Lugones, *Radial Oscillations of Color Superconducting Self-Bound Quark Stars*, Phys. Rev. D **82**, 063006 (2010).
22. J. D. V. Arbañil and M. Malheiro, *Radial Stability of Anisotropic Strange Quark Stars*, J. Cosmol. Astropart. Phys. **11**, 012 (2016).
23. J. D. V. Arbañil, C. V. Flores, C. H. Lenzi and J. M. Z. Pretel, *Fluid Pulsation Modes and Tidal Deformability of Anisotropic Strange Stars in Light of the GW170817 Event*, Phys. Rev. D **107**, 124016 (2023).
24. C. Alcock, E. Farhi and A. Olinto, *Strange Stars*, Astrophys. J. **310**, 261–272 (1986).
25. P. Haensel, J. L. Zdunik and R. Schaeffer, *Strange Quark Stars*, Astron. Astrophys. **160**, 121–128 (1986).
26. A. R. Bodmer, *Collapsed Nuclei*, Phys. Rev. D **4**, 1601–1606 (1971).
27. E. Witten, *Cosmic Separation of Phases*, Phys. Rev. D **30**, 272–285 (1984).
28. E. Farhi and R. L. Jaffe, *Strange Matter*, Phys. Rev. D **30**, 2379–2390 (1984).
29. X.-D. Li, I. Bombaci, M. Dey, J. Dey and E. P. J. van den Heuvel, *Is SAX J1808.4−3658 a Strange Star?*, Phys. Rev. Lett. **83**, 3776–3779 (1999).
30. J. J. Drake et al., *Is RX J1856.5−3754 a Quark Star?*, Astrophys. J. **572**, 996–1001 (2002).
31. M. G. Alford, S. Han and M. Prakash, *Generic Conditions for Stable Hybrid Stars*, Phys. Rev. D **88**, 083013 (2013).
32. D. Leahy and R. Ouyed, *Supernova SN2006gy as a First Ever Quark Nova?*, Mon. Not. R. Astron. Soc. **387**, 1193–1198 (2008).
33. B. Paczyński and P. Haensel, *Gamma-ray Bursts from Quark Stars*, Mon. Not. R. Astron. Soc. **362**, L4–L7 (2005).
34. A. Bauswein, R. Oechslin and H.-T. Janka, *Discriminating Strange Star Mergers from Neutron Star Mergers by Gravitational-wave Measurements*, Phys. Rev. D **81**, 024012 (2010).
35. D. Page and V. V. Usov, *Thermal Evolution and Light Curves of Young Bare Strange Stars*, Phys. Rev. Lett. **89**, 131101 (2002).
36. A. Chodos, R. L. Jaffe, K. Johnson, C. B. Thorn and V. F. Weisskopf, *New Extended Model of Hadrons*, Phys. Rev. D **9**, 3471–3495 (1974).
37. J. L. Zdunik, *Strange Stars: Linear Approximation of the Equation of State and Maximum QPO Frequency*, Astron. Astrophys. **359**, 311–315 (2000).
38. M. G. Alford, G. F. Burgio, S. Han, G. Taranto and D. Zappalà, *Constraining and Applying a Generic High-Density Equation of State*, Phys. Rev. D **92**, 083002 (2015).

39. R. L. Bowers and E. P. T. Liang, *Anisotropic Spheres in General Relativity*, Astrophys. J. **188**, 657–665 (1974).
40. M. Ruderman, *Pulsars: Structure and Dynamics*, Annu. Rev. Astron. Astrophys. **10**, 427–476 (1972).
41. V. Canuto and J. Ventura, *Quantizing Magnetic Fields in Astrophysics*, Fundam. Cosmic Phys. **2**, 203–353 (1977).
42. L. Herrera and N. O. Santos, *Local Anisotropy in Self-Gravitating Systems*, Phys. Rep. **286**, 53–130 (1997).
43. B. V. Ivanov, *Maximum Bounds on the Surface Redshift of Anisotropic Stars*, Phys. Rev. D **65**, 104011 (2002).
44. D. D. Doneva and S. S. Yazadjiev, *Non-Radial Oscillations of Anisotropic Neutron Stars in the Cowling Approximation*, Phys. Rev. D **85**, 124023 (2012).
45. D. Deb, B. Mukhopadhyay and F. Weber, *Effects of Anisotropy on Strongly Magnetized Neutron and Strange Quark Stars in General Relativity*, Astrophys. J. **922**, 149 (2021).
46. L. Herrera, *Stability of the isotropic pressure condition*, Phys. Rev. D **101**, 104024 (2020).
47. K. Dev and M. Gleiser, *Anisotropic Stars: Exact Solutions*, Gen. Relativ. Gravit. **34**, 1793–1818 (2002).
48. K. Dev and M. Gleiser, *Anisotropic Stars II: Stability*, Gen. Relativ. Gravit. **35**, 1435–1457 (2003).
49. D. Horvat, S. Ilijić and A. Marunović, *Radial Pulsations and Stability of Anisotropic Stars with a Quasi-Local Equation of State*, Class. Quantum Grav. **28**, 025009 (2011).
50. R. C. Tolman, *Static Solutions of Einstein's Field Equations for Spheres of Fluid*, Phys. Rev. **55**, 364–373 (1939).
51. H. A. Buchdahl, *General Relativistic Fluid Spheres*, Phys. Rev. **116**, 1027–1034 (1959).
52. K. Lake, *All Static Spherically Symmetric Perfect-Fluid Solutions of Einstein's Equations*, Phys. Rev. D **67**, 104015 (2003).
53. L. Herrera, *New Definition of Complexity for Self-Gravitating Fluid Distributions: The Spherically Symmetric, Static Case*, Phys. Rev. D **97**, 044010 (2018).
54. S. K. Maurya and F. Tello-Ortiz, *Generalized Relativistic Anisotropic Compact Star Models by Gravitational Decoupling*, Eur. Phys. J. C **79**, 85 (2019).
55. J. Ovalle, *Searching Exact Solutions for Compact Stars in Braneworld: A Conjecture*, Mod. Phys. Lett. A **23**, 3247–3263 (2008).
56. J. Ovalle, *Decoupling Gravitational Sources in General Relativity: From Perfect to Anisotropic Fluids*, Phys. Rev. D **95**, 104019 (2017).
57. J. Ovalle, R. Casadio, R. da Rocha and A. Sotomayor, *Anisotropic Solutions by Gravitational Decoupling*, Eur. Phys. J. C **78**, 122 (2018).
58. J. Ovalle, *Decoupling Gravitational Sources in General Relativity: The Extended Case*, Phys. Lett. B **788**, 213–218 (2019).
59. L. Gabbanelli, Á. Rincón and C. Rubio, *Gravitational Decoupled Anisotropies in Compact Stars*, Eur. Phys. J. C **78**, 370 (2018).
60. E. Contreras and P. Bargueño, *Minimal Geometric Deformation in Asymptotically (A-)dS Space-Times and the Isotropic Sector for a Polytropic Black Hole*, Eur. Phys. J. C **78**, 985 (2018).
61. G. Abellán, Á. Rincón, E. Fuenmayor and E. Contreras, *Anisotropic Interior Solution by Gravitational Decoupling Based on a Non-Standard Anisotropy*, Eur. Phys. J. Plus **135**, 606 (2020).
62. P. León, E. Fuenmayor and E. Contreras, *Gravitational Cracking of General Relativistic Polytropes: A Generalized Scheme*, Phys. Rev. D **104**, 044053 (2021).
63. D. Santana, E. Fuenmayor and E. Contreras, *Integration of the Lane–Emden Equation for Relativistic Anisotropic Polytropes through Gravitational Decoupling: A Novel Approach*, Eur. Phys. J. C **82**, 703 (2022).
64. J. Andrade et al., *Gravitational Decoupled Interior Solutions from Kohler–Chao–Tikekar Cosmological Model*, Eur. Phys. J. C **84**, 533 (2024).
65. T. Naseer, M. Sharif, A. Tehreem and J. Andrade, *Polytropes in general relativity under minimal gravitational decoupling*, Phys. Lett. A **580**, 131518 (2026).
66. J. Andrade, D. Santana, T. Naseer, E. Pozo Valdiviezod and D. T. Castañeda Ortiz, *Implications of gravitational decoupling on energy exchange of extended Einstein's universe solution*, Eur. Phys. J. C **85**, 1174 (2025).
67. J. Andrade and E. Contreras, *Stellar models with like-Tolman IV complexity factor*, Eur. Phys. J. C **81**, 889 (2021).
68. B. Siza, J. Andrade, D. Santana and T. Naseer, *Anisotropic extension of the Kohler–Chao–Tikekar cosmological solution with like Wyman IIa complexity factor*, Eur. Phys. J. C **84**, 1203 (2024). doi:10.1140/epjc/s10052-024-13591-y.
69. S. Chandrasekhar, *The Dynamical Instability of Gaseous Masses Approaching the Schwarzschild Limit in General Relativity*, Astrophys. J. **140**, 417–433 (1964).
70. S. Chandrasekhar, *A General Variational Principle Governing the Radial and Non-Radial Oscillations of Gaseous Masses*, Astrophys. J. **139**, 664–674 (1964).
71. D. Gondek, P. Haensel and J. L. Zdunik, *Radial Pulsations and Stability of Protoneutron Stars*, Astron. Astrophys. **325**, 217–227 (1997).
72. K. D. Kokkotas and B. G. Schmidt, *Quasi-Normal Modes of Stars and Black Holes*, Living Rev. Relativ. **2**, 2 (1999).
73. P. Luz and S. Carloni, *Adiabatic Radial Perturbations of Relativistic Stars: Analytic Solutions to an Old Problem*, Phys. Rev. D **110**, 084054 (2024).
74. G. Panotopoulos and I. Lopes, *Radial Oscillations of Strange Quark Stars Admixed with Condensed Dark Matter*, Phys. Rev. D **96**, 083013 (2017).
75. J. C. Jiménez and E. S. Fraga, *Radial Oscillations of Quark Stars from Perturbative QCD*, Phys. Rev. D **100**, 114041 (2019).
76. J. Bora and U. D. Goswami, *Radial Oscillations and Gravitational Wave Echoes of Strange Stars for Various Equations of State*, Mon. Not. R. Astron. Soc. **502**, 1557–1568 (2021).
77. S. R. Mohanty, S. Ghosh and B. Kumar, *Unstable Anisotropic Neutron Stars: Probing the Limits of Gravitational Collapse*, Phys. Rev. D **109**, 123039 (2024).
78. G. Darmois, *Les èquations de la gravitation einsteinienne*, Mémorial des Sciences Mathématiques, Vol. 25 (Gauthier-Villars, Paris, 1927).
79. W. Israel, *Singular hypersurfaces and thin shells in general relativity*, Nuovo Cimento B **44**, 1–14 (1966).
80. G. Lugones and J. E. Horvath, *Color-Flavor Locked Strange Matter*, Phys. Rev. D **66**, 074017 (2002).
81. T. Harko and K. S. Cheng, *Maximum Mass and Radius of Strange Stars in the Linear Approximation of the Equation of State*, Astron. Astrophys. **385**, 947–950 (2002).
82. Ya. B. Zel'dovich, *The Equation of State at Ultrahigh Densities and Its Relativistic Limitations*, Sov. Phys. JETP **14**, 1143–1147 (1962).
83. C. E. Rhoades, Jr. and R. Ruffini, *Maximum Mass of a Neutron Star*, Phys. Rev. Lett. **32**, 324–327 (1974).
84. H. C. Das and L. L. Lopes, *Anisotropic strange stars in the spotlight: unveiling constraints through observational data*, Mon. Not. R. Astron. Soc. **525**, 3571–3575 (2023).

85. J. M. Z. Pretel, T. Tangphati, A. Banerjee and A. Pradhan, *Effects of anisotropic pressure on interacting quark star structure*, Phys. Lett. B **848**, 138375 (2024).
86. S. Mondal and M. Bagchi, *Quasinormal f-modes of anisotropic quark stars in full general relativity*, Phys. Rev. D **111**, 103035 (2025).
87. G. Panotopoulos, *On modeling anisotropic quark stars: the role of anisotropy in radial oscillation spectra*, Symmetry **18**, 1295 (2026).
88. T. Gangopadhyay, S. Ray, X.-D. Li, J. Dey and M. Dey, *Strange star equation of state fits the refined mass measurement of 12 pulsars and predicts their radii*, Mon. Not. R. Astron. Soc. **431**, 3216–3221 (2013).